Central Lancashire Online Knowledge (CLoK)

Title	A low-mass hub-filament with double centre revealed in NGC2071-North
Type	Article
URL	https://clok.uclan.ac.uk/45413/
DOI	https://doi.org/10.1093/mnras/stad132
Date	2023
Citation	Könyves, Vera, Ward-Thompson, Derek, Shimajiri, Y, Palmeirim, P and André, Ph (2023) A low-mass hub-filament with double centre revealed in NGC2071-North. Monthly Notices of the Royal Astronomical Society. ISSN 0035-8711
Creators	Könyves, Vera, Ward-Thompson, Derek, Shimajiri, Y, Palmeirim, P and André, Ph

Monthly Notices
of the
ROYAL ASTRONOMICAL SOCIETY

MNRAS **520,** 4646–4663 (2023)
Advance Access publication 2023 January 14

https://doi.org/10.1093/mnras/stad132

A low-mass hub–filament with double centre revealed in NGC 2071-North

Vera Könyves ,[1★] D. Ward-Thompson ,[1] Y. Shimajiri,[2,3] P. Palmeirim [4] and Ph. André[5]

[1] *Jeremiah Horrocks Institute, University of Central Lancashire, Preston PR1 2HE, UK*
[2] *National Astronomical Observatory of Japan, National Institutes of Natural Sciences, 2-21-1 Osawa, Mitaka, Tokyo 181-8588, Japan*
[3] *Kyushu Kyoritsu University, Jiyugaoka 1-8, Yahatanishi-ku, Kitakyushu, Fukuoka 807-8585, Japan*
[4] *Instituto de Astrofísica e Ciências do Espaço, Universidade do Porto, CAUP, Rua das Estrelas, P-4150-762 Porto, Portugal*
[5] *Laboratoire d'Astrophysique (AIM), CEA, CNRS, Université Paris-Saclay, Université Paris Diderot, Sorbonne Paris Cité, F-91191 Gif-sur-Yvette, France*

Accepted 2022 December 31. Received 2022 December 31; in original form 2021 December 22

ABSTRACT

We present the first analysis in NGC 2071-North as a resolved hub–filament featuring a double centre. This $\sim$1.5 × 1.5 pc^2 scale filament hub contains $\sim$500 M$_\odot$. Seen from *Planck*, magnetic field lines may have facilitated the gathering of material at this isolated location. The energy balance analysis, supported by infalling gas signatures, reveals that these filaments are currently forming stars. *Herschel* 100 μm emission concentrates in the hub, at IRAS 05451+0037 and LkHα 316, and presents diffuse lobes and loops around them. We suggest that such a double centre could be formed, because the converging locations of filament pairs are offset, by 2.3 arcmin (0.27 pc). This distance also matches the diameter of a hub ring, seen in column density and molecular tracers, such as HCO$^+$ (1–0) and HCN (1–0), that may indicate a transition and the connection between the hub and the radiating filaments. We argue that all of the three components of the emission star LkHα 316 are in physical association. We find that a $\sim$0.06-pc-sized gas loop, attached to IRAS 05451+0037, can be seen at wavelengths all the way from the Panoramic Survey Telescope and Rapid Response System (Pan-STARRS)-*i* to *Herschel* 100 μm. These observations suggest that both protostars at the double hub centre are interacting with the cloud material. In our ^{13}CO data, we do not seem to find the outflow of this region that was identified in the 1980s with much lower resolution.

Key words: galaxies: star formation – ISM: clouds – ISM: individual objects: NGC 2071-North – ISM: structure.

1 INTRODUCTION

Thanks to recent space-based (e.g. *Herschel*) and sensitive ground-based (e.g. Atacama Large Millimeter/submillimeter Array (ALMA) and Expanded Very Large Array (EVLA)) observations, much progress is being made on the early stages of star formation. This is being achieved by not only looking at the very peak of such sources, but also considering their near and far surroundings in the molecular clouds that are forming stars. In particular, many studies have shown that the cold material of molecular clouds is often organized in networks of filaments, whether these clouds are currently forming stars or not (e.g. Arzoumanian et al. 2011, 2019). Most of the clumps and cores are seen forming in these filaments (e.g. André et al. 2014; Könyves et al. 2015, 2020), the formation of which may be due to various mechanisms, invoking one or more of the turbulent-, gravitational-, and magnetic forces. Summaries on the origin of interstellar filaments can be found in André et al. (2014), Hacar et al. (2022), and Pineda et al. (2022).

Nearby *Herschel* filaments – up to $\sim$0.5 kpc distance – appear to be characterized by a narrow distribution of transverse half-power widths with a typical full width at half-maximum (FWHM) value of 0.1 pc (e.g. Arzoumanian et al. 2011, 2019; Koch & Rosolowsky 2015). While there has been some debate about the reliability of this finding (cf. Panopoulou et al. 2022), tests performed on synthetic data suggest that published *Herschel* width measurements are not affected by significant biases, at least in the case of nearby, high-contrast filamentary structures (Arzoumanian et al. 2019; André, Palmeirim & Arzoumanian 2022).

The Orion B cloud complex at $d \sim 400$ pc (Menten et al. 2007; Lallement et al. 2014; Zucker et al. 2019) was studied by the *Herschel* Gould Belt Survey (HGBS; André et al. 2010). Here, Könyves et al. (2020) confirmed the physical existence of a transition in pre-stellar core formation efficiency (CFE) around a fiducial threshold of $A_{\rm V}^{\rm bg} \sim$ 7 mag in background visual extinction. This is similar to the trend observed with *Herschel* in other regions, such as the Aquila cloud (Könyves et al. 2015). Between $A_{\rm V}^{\rm bg} \sim 5$ and 10 mag the CFE goes steeply from low to high, and the bulk of core and star formation is occurring above this threshold that had already been suspected earlier (e.g. Onishi et al. 1998; Johnstone, Di Francesco & Kirk 2004; Kirk, Johnstone & Di Francesco 2006). In the filamentary regions of NGC 2023/24, NGC 2068/71 (see Fig. 1, left) and the L1622 cometary cloud, Könyves et al. (2020) found a total of 1768 starless cores ($\sim$28–45 per cent of which are gravitationally bound pre-stellar cores) and an additional 76 protostellar (Class 0–I) cores. In Orion B, the mass in pre-stellar cores above the mentioned threshold represents only a moderate fraction ($\sim$20 per cent); and $\sim$60–80 per cent of the gravitationally bound cores are associated with filaments.

Interstellar filaments also play an important role in the formation of massive stars, where these dense elongated features are often organized in a 'hub–filament' structure with converging arms (e.g. Myers 2009; Peretto et al. 2013). Similar structures were called

---

★ E-mail: vera.konyves@gmail.com

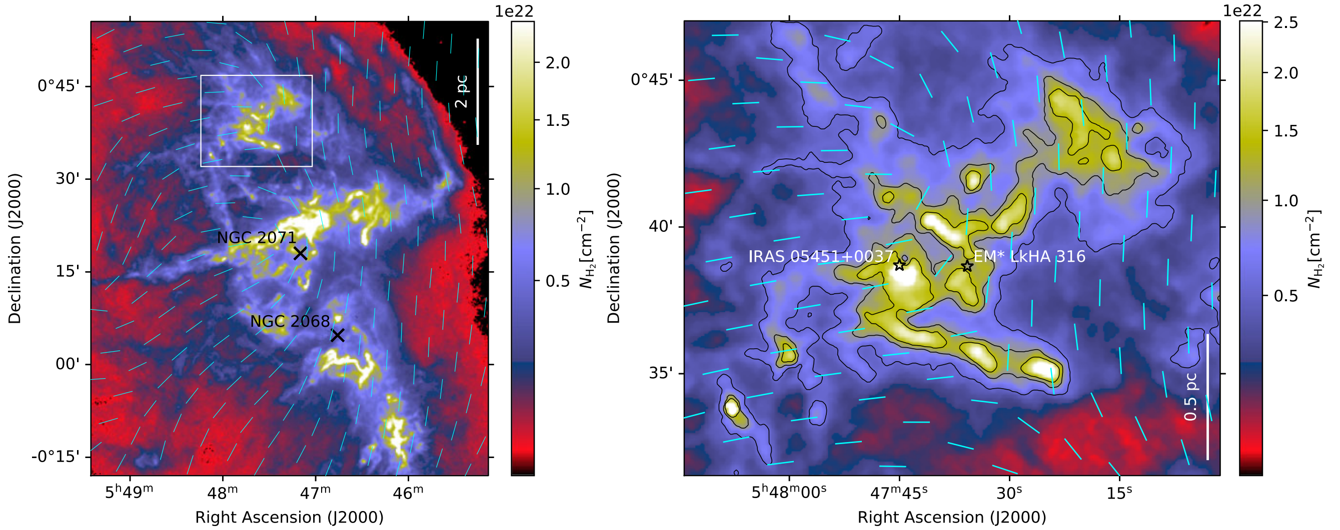

Figure 1. Left: column density map of Orion B showing the region around NGC 2071 (see Könyves et al. 2020). The white square outlines a ∼18 × 15 arcmin^2 field centred on RA = 05:47:37.8, Dec. = +00:39:16. The column density peak within this box, somewhat lower left from the centre, corresponds to $\sim 4 \times 10^{22}$ cm^{-2}, where the dust filaments exhibit a multi-arm hub morphology. Right: zoomed column density map on the filament hub, marking the locations of two embedded protostars. Black contours correspond to $N_{H_2} = [5.5 \times 10^{21}, 9.7 \times 10^{21}, 1.4 \times 10^{22}]$ cm^{-2}, which are equivalent to ∼6, 10, and 15 mag of visual extinction. The same contours are used in subsequent figures. In both panels *Planck B*-field-oriented vectors are overplotted in cyan on a 5-arcmin scale (left), and 1.71-arcmin scale (right).

‘junctions of filaments’ by Schneider et al. (2012), who found that massive clusters more likely lie in the proximity of junctions of filaments in high column density regions, as Dale & Bonnell (2011) proposed from simulations.

Clumps with radiating multiple filaments can be seen in low-mass star-forming fields as well (e.g. in Pipe Nebula; Peretto et al. 2012). However, single filaments that do not cross each other (e.g. in Taurus; Palmeirim et al. 2013) appear to provide enough material to form solar-type stars. The hub–filament mode may be more typical, and its role may be more important, in regions of massive star formation, where the hub centre represents a deep potential well, able to accrete much more material from the surrounding filaments.

As for the role of the magnetic field (*B* field) in the formation and evolution of such structures, a bimodal distribution of the relative orientations between the filaments and the mean magnetic field directions was found observationally, i.e. these relative orientations change from parallel to perpendicular with increasing (column) density. In other words, the relative orientations between the *B* fields and the elongated structures were found to be mostly parallel in low-density filaments, and mostly perpendicular in dense filaments. These structures can be matched to the lower density ‘parallel’ filaments and the high-density elongated hubs they are connected to in the hub–filament model by Myers (2009). Li et al. (2013) showed from observations that uniform (i.e. dynamically important) *B* fields on larger scales can give rise to typical hub–filament cloud morphology. A strong interplay and the bimodality between interstellar *B* fields and filaments were also shown by Planck Collaboration XXXV (2016) and Alina et al. (2019), after these have been predicted by magnetohydrodynamic (MHD) simulations (Nakamura & Li 2008; Soler et al. 2013; Chen, King & Li 2016; Soler & Hennebelle 2017).

The region of interest of this work is a so far poorly studied subregion north of NGC 2071 that was named ‘NGC 2071-North’ (see Fig. 1, right) by Iwata, Fukui & Ogawa (1988). They made molecular observations in ^{12}CO, ^{13}CO, C^{18}O (1–0), and NH$_3$ (1, 1) and (2, 2) lines, and followed up a CO outflow, discovered by Fukui et al. (1986). This relatively old ($t \sim 1.7 \times 10^5$ yr) outflow shows a U-shape, and is apparently driven by IRAS 05451+0037. This was confirmed by Goldsmith et al. (1992) with 3 mm wavelength molecular observations. They argued that the molecular abundances in NGC 2071-North (or NGC 2071-N) have been significantly affected by this outflow and the presence of young stellar objects (YSOs). With this study we follow on from Gibb (2008), who also summarized the findings in NGC 2071-N up to 2008.

As we mentioned above, cloud material may be channelled more efficiently through filaments into the seeds of star formation. However, newly formed luminous sources can also significantly alter the geometry and composition of the surrounding material. While massive young stars can have dramatic effects on their neighbourhood by ionization and major dynamical impact (H II regions; e.g. Tenorio-Tagle 1982), winds and outflows of lower mass young stars can also sweep up gas and dust by injecting considerable mechanical energy into the interstellar medium (ISM; cf. Snell 1989). All of these feedback effects, which are an integral part of the star formation process, can trigger temperature and density changes in the surrounding matter.

Aspin & Reipurth (2000) performed optical CCD imaging around compact reflection nebulae and embedded *Infrared Astronomical Satellite* (*IRAS*) sources in order to search for new Herbig–Haro (HH) jets and flows. They also identified a cluster of new HH objects associated with IRAS 05451+0037 and the nearby young star LkHα 316 in the centre of NGC 2071-N.

Hillenbrand et al. (2012) detected strong emission-line features in the TiO and VO bands at the position of the optically faint, flat-spectrum protostar IRAS 05451+0037 too, which suggests that it may be surrounded by dense and warm circumstellar gas.

Because of its relative isolation north of NGC 2071 (see Fig. 1, left), this subregion is still not well studied. We present here the first analysis of NGC 2071-N with high-resolution data sets of both the extended molecular material and the compact star-forming cores. It was hypothesized that it was once an elongated molecular clump along the east–west and south-east–north-west directions (Iwata et al.

1988; Goldsmith et al. 1992), and that NGC 2071-North has now been refined into a 'filamentary hub' structure.

This paper is organized as follows. Section 2 provides details about the used data sets. In Section 3, we show distance results from *Gaia* Early Data Release 3 (EDR3) measurements, *Herschel*-derived properties, molecular line-derived properties, and we also estimate the energy balance based on energy densities and pressures. In Section 4, we discuss the large-scale magnetic field over NGC 2071-N, we reason that star formation is ongoing here, we discuss the double centre, and revisit the existence of a CO outflow in the region. Finally, Section 5 presents our conclusions.

2 OBSERVATIONS AND DATA

2.1 *Herschel* data

In this study, we used part of the Spectral and Photometric Imaging REceiver (SPIRE) and Photodetector Array Camera and Spectrometer (PACS) 'parallel-mode' HGBS observations of the Orion B complex that includes NGC 2071-N (see André et al. 2010). The details of the data-reduction process are discussed by Könyves et al. (2020). In this work, we used the SPIRE 250-μm data, calibrated in MJy sr^{-1}, on 3 arcsec pixel scales. We also used the H_2 column density map that was created from the HGBS observations[1] (see Könyves et al. 2020).

In addition, we used PACS-only mode 100-μm, and 160-μm data, also from the HGBS project (OBSIDs: 1342206054, 1342206055), observed on 2010 October 8 with a scanning speed of 20 arcsec s^{-1} (as opposed to the parallel-mode's 60 arcsec s^{-1}). They were reduced in the same way as the parallel-mode PACS observations (see Könyves et al. 2020).

2.2 IRAM 30-m observations

In the 2013 summer semester, we carried out the Institut de Radioastronomie Millimetrique (IRAM) 30-m observations under project number 030–13. We used the Eight MIxer Receiver (EMIR; Carter et al. 2012) at 3 mm to take fully sampled $C^{18}O$ (1–0) and ^{13}CO (1–0) maps simultaneously in a ∼108 arcmin^2 region towards NGC 2071-N. The on-the-fly mapping mode was used with position switching. At 109.782 GHz, the 30-m telescope has a beam size of 23.6 arcsec and the forward and main beam (MB) efficiencies (F_{eff} and B_{eff}) are 95 per cent and 79 per cent, respectively. The backend used was the VESPA autocorrelator providing a frequency resolution of 20 kHz that corresponds to ∼0.055 km s^{-1} in velocity resolution.

For the position-switching mode, the reference position was offsetted by ∼20 arcmin from the map centre. The off position was selected from *Herschel* column density images, and we made sure that no significant CO emission is appearing there by observations in frequency-switching mode.

During the observations, calibration was performed every ∼30 min, and the telescope pointing was checked and adjusted every ∼2 h. The pointing accuracy was found to be better than 3 arcsec. All of the data were reduced with the GILDAS/CLASS software package.[2]

We smoothed the data spatially with a Gaussian function resulting in an effective beam size of 28 arcsec (∼0.05 pc at ∼400 pc). The 1σ noise level of the final mosaicked data cube is ∼0.11 K in T_{MB}, at an effective angular resolution of 28 arcsec and a velocity resolution of ∼0.1 km s^{-1}.

2.3 NRO 45-m observations

In 2015, we carried out observations on the 45-m telescope of the Nobeyama Radio Observatory (NRO) towards a 0.14 deg^2 region in the Orion B cloud, including the densest portions of NGC 2071-North, with the TZ receiver (Shimajiri et al. 2017). All molecular line data (HCN (1–0), $H^{13}CN$ (1–0), HCO^+ (1–0), and $H^{13}CO^+$ (1–0)) were obtained simultaneously. At 86 GHz, the telescope has a beam size of 19.1 arcsec (half-power beamwidth – HPBW) and a main beam efficiency of ∼50 per cent. As a backend, we used the Spectral Analysis Machine for the 45-m telescope (SAM45) spectrometer, which provides a bandwidth of 31 MHz and a frequency resolution of 7.63 kHz. The latter corresponds to a velocity resolution of ∼0.02 km s^{-1} at 86 GHz. We applied spatial smoothing to the data with a Gaussian function resulting in an effective beam size of 30 arcsec. The 1σ noise level of the final data is ∼0.35 K in T_{MB} at an effective resolution of 30 arcsec and a velocity resolution of 0.1 km s^{-1}. More details of these observations and data reduction are described by Shimajiri et al. (2017).

Some image operations, such as *moment* and *smooth*, were performed using the MIRIAD software package (Sault, Teuben & Wright 1995), for both the NRO and the IRAM observations.

2.4 Archival data

In order to trace and visualize NGC 2071-North, in particular the central part of the hub, we have displayed and superimposed various data sets and catalogues within the interactive software ALADIN sky atlas[3] (Bonnarel et al. 2000).

In addition to the above data sets, then we downloaded high-resolution short-wavelength Sloan Digital Sky Survey (SDSS), Panoramic Survey Telescope and Rapid Response System (Pan-STARRS), and Two Micron All Sky Survey (2MASS) images to further trace the interesting structures that we first caught in the 100 μm map.

SDSS images were retrieved from the SkyView Query Form[4] that service resampled the data from the SDSS[5] (Eisenstein et al. 2011). In this work, we visualize SDSS data observed with the *g*, *r*, and *i* colour filters.

2MASS[6] (Skrutskie et al. 2006) *J*, *H*, and K_{s} infrared images were also queried from NASA's SkyView service.

Pan-STARRS is a system for wide-field astronomical imaging developed and operated by the Institute for Astronomy at the University of Hawaii. We downloaded Data Release 2 (DR2) data of the first part of the project (Chambers et al. 2016) to be completed through their Image Cutout Service[7]. Out of the five broad-band filters (*g*, *r*, *i*, *z*, and *y*), we used *i*, *z*, and *y*.

To double-check the distance measurements in this region, we used *Gaia* EDR3 sources (Gaia Collaboration 2018) downloaded from the *Gaia* Archive[8].

---

[1] http://gouldbelt-herschel.cea.fr/archives

[2] http://www.iram.fr/IRAMFR/GILDAS

[3] http://aladin.u-strasbg.fr

[4] https://skyview.gsfc.nasa.gov

[5] www.sdss3.org

[6] https://irsa.ipac.caltech.edu/Missions/2mass.html

[7] https://ps1images.stsci.edu/cgi-bin/ps1cutouts

[8] http://gea.esac.esa.int/archive

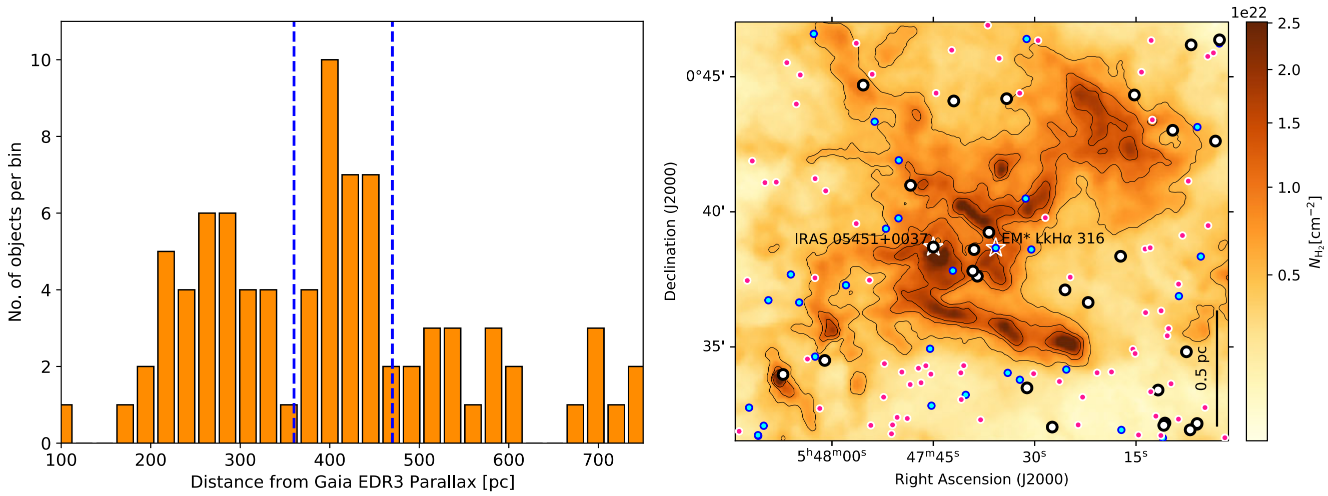

Figure 2. Left: histogram of distances converted from *Gaia* EDR3 parallax measurements over the region shown in the right-hand panel. Dashed blue lines mark the distances at 360 and 470 pc (see text for details). Right: overlaid on column density, cyan/blue dots mark the *Gaia* measurement points at $d < 360$ pc, white/black dots show the positions of $d = 360$–470 pc measurements, which are a priori considered Orion B sources, and magenta/white dots mark the locations of *Gaia* EDR3 sources beyond 470 pc. Again, white stars mark the two named protostars.

3 RESULTS AND ANALYSIS

3.1 Distance from *Gaia* EDR3 data

The most prominent features within Orion B are the Horsehead Nebula, the NGC 2023/24, and NGC 2068/71 nebulae, as well as the Lynds 1622 (L1622) cometary cloud north-east of NGC 2071-North (see fig. 2 of Könyves et al. 2020). In the Lynds catalogue L1630 covers Orion B without L1622. As it was mentioned in Section 1, we consider $d \sim 400$ pc for the distance to most of the Orion B clouds (Anthony-Twarog 1982; Menten et al. 2007; Gibb 2008; Lallement et al. 2014; Schlafly et al. 2014; Zucker et al. 2019), while there is indication that the cometary, trunk-like features at and around L1622 may not be at this same distance. The alignment of the trunks and comets suggests that this northern part of Orion B interacts with the Barnard's Loop (see fig. 1 of Könyves et al. 2020). Thus, the L1622 region may also be at a closer distance (∼170–180 pc), which is tentatively found for Barnard's Loop by Bally (2008) and Lallement et al. (2014). However, its distance is still uncertain (see e.g. Ochsendorf et al. 2015, and references therein).

Revisiting fig. 1 of Könyves et al. (2020) gave the idea to check the distances at NGC 2071-N with available *Gaia* EDR3 data, as the Hα shell of Barnard's Loop seems to cut through Orion B between NGC 2071 and L1622.

Gaia EDR3 measurements have been downloaded for the coverage shown in, for example, Fig. 1, right, from which we only exploited RA(J2000) and Dec.(J2000) coordinates, parallax, and parallax errors. Distances in parsec from the parallax data (in arcsec) have been converted with ASTROPY's *to*() unit conversion method (Greenfield et al. 2013). For the analysis, we ignored data points with negative parallax, as well as data where the parallax error was larger than half of the parallax value.

The histogram in the left-hand panel of Fig. 2 shows the distances for the region in the right-hand panel. A significant group of distances around 400 pc is apparent. However, a very wide range of distances is found in this ∼18 × 15 arcmin^2 region. From the histogram, we set lower and upper distance limits around Orion B, at 360 and 470 pc, which seem to be reasonable choices, and they may also indicate a cloud depth, at NGC 2071-N, of about 100 pc. The *Gaia* data points in these three distance ranges are plotted in Fig. 2, right. The cyan/blue dots mark the positions of *Gaia* measurements up to 360 pc, the white/black dots show the a priori Orion B sources between 360 and 470 pc, and the sources beyond 470 pc are marked with magenta/white dots. These latter ones most probably belong to the background, as they almost only appear where the cloud is more transparent (i.e. with less column density). A group of white/black dots at around 400 pc is concentrated in the central portion of the hub and/or at higher column densities, which is reassuring. More of them also show up in the lower right-hand corner that is in the direction of NGC 2071. However, the cyan/blue dots appear everywhere in the line of sight, and apparently the nebulous star LkHα 316 also seems to lie closer to us than 360 pc.

Distances from EDR3 parallaxes of the two central objects, IRAS 05451+0037 and LkHα 316, gave us $d_{\rm IRAS} = 383.4^{+15.3}_{-14.2}$ pc and $d_{\rm LkH\alpha} = 300.6^{+48.2}_{-36.5}$ pc, respectively, at which distances they may still belong to the same cloud.

After the above filtering of *Gaia* EDR3 measurement points, the distances range from ∼100 to 6300 pc. They all are plotted in Fig. 2, right, while only those up to ∼800 pc are shown in the left-hand side histogram.

3.2 *Herschel* properties of the hub–filament

The spectacular hub–filament structure of NGC 2071-North, seen in, for instance, Fig. 3 is made up of high column density multi-arms, corresponding to equivalent visual extinctions of $A_{\rm V} \gtrsim 5$. It is relatively isolated from NGC 2071, thus this subregion is still not much studied. It occupies a ∼1.5 × 1.5 pc^2 projected area at a distance of ∼400 pc, and it was identified as such a structure in HGBS images (Könyves et al. 2020).

We have studied the star-forming properties of these filaments in Könyves et al. (2020), where the dense core population of the whole Orion B cloud was discussed, also with respect to filaments (see Fig. 3, left). The mass of the NGC 2071-North structure is found to be about 500 M$_\odot$ above $A_{\rm V} \sim 5$ mag that is less than that of the Serpens-South filament hub; ∼750 M$_\odot$ in a ∼1 × 2 pc^2 region, most of which is even above $A_{\rm V} \sim 10$ mag, assuming a distance of 260 pc (Könyves et al. 2015). On the other hand, the B59 filament hub in

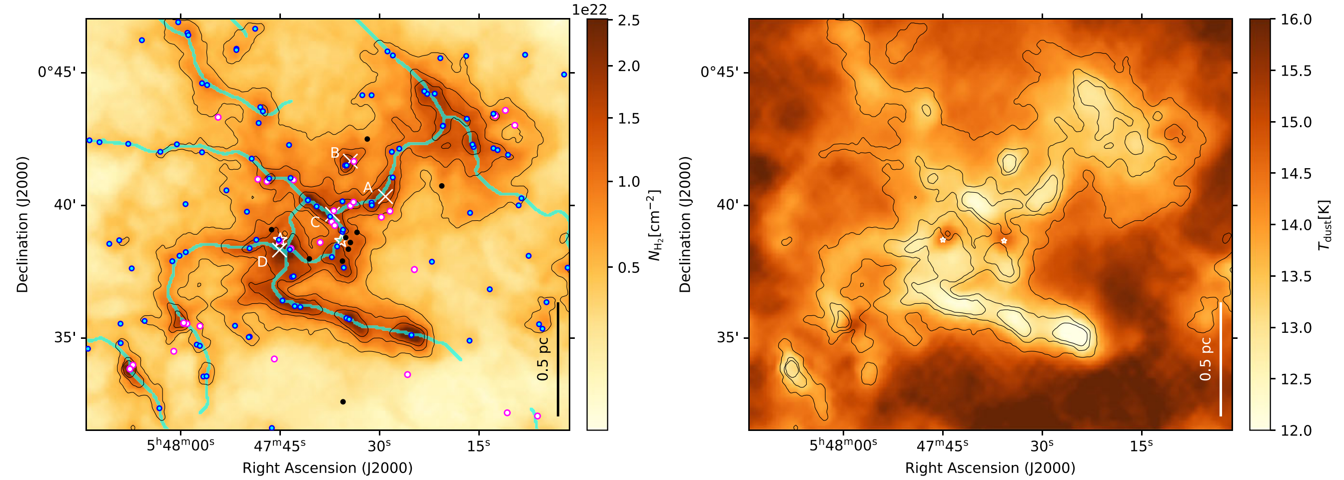

Figure 3. Left: column density map of the NGC 2071-N filament hub, with DisPerSE (Sousbie 2011) filaments. Dense cores (bound pre-stellar and unbound starless) from Kirk et al. (2016) and Könyves et al. (2020) are overplotted with cyan/blue dots. White/magenta dots mark YSOs/protostars from SIMBAD together with a few embedded protostars from Könyves et al. (2020). Black dots mark Herbig–Haro (HH) objects from SIMBAD. Four white crosses show the positions of NH_3 (1, 1) cores defined by Iwata et al. (1988). Right: dust temperature map of the same region. Maps and filaments are from Könyves et al. (2020). In both panels, the left- and right-hand white stars (also protostars) mark the locations of IRAS 05451+0037 and LkHα 316, respectively.

Pipe (Peretto et al. 2012) is at lower extinction, its mass above $A_V \sim 5$ is only $\sim$30 M$_{\odot}$ (covering the hub centre and one filament arm).

Dust temperatures, also derived from HGBS data, within the lowest contours in the column density map at 5.5×10^{21} cm^{-2} are found to be $\sim$14 K or less (see Fig. 3, right). Within the densest portions (southern filament, clumps A, B, C, north-west corner) the temperature drops below 13 K, while the direct surroundings (within $\sim$20 arcsec) of the two central protostars exhibit temperatures between 14 and 15 K.

The bound pre-stellar core masses are in the range of $\sim$0.2–10 M$_{\odot}$ with a median mass of $\sim$1 M$_{\odot}$, which would eventually collapse to low-mass stars. These sources are also among the overplotted ones in Fig. 3, left. The properties around them, together with further derived properties from Section 3.4, are listed in Table 1. In Fig. 3, left, it is clear that most of the dense cores (cyan/blue dots) are located along filaments and elongated features. This tendency has been noted and discussed in several HGBS papers (e.g. André et al. 2014; Marsh et al. 2016; Benedettini et al. 2018; Ladjelate et al. 2020; Fiorellino et al. 2021), and this result does not depend significantly on the method of filament extraction (Könyves et al. 2020). This same figure panel also shows that YSOs and protostars (white/magenta dots) tend to appear at locations that are at the crossing points of filaments. For instance, at core C and D of Iwata et al. (1988) (identified from NH_3 (1, 1) observations), which are at the junction of extracted cyan filaments. A similar effect on larger scales, that infrared clusters are found at the junction of filaments, has been found by several studies (Myers 2009; Schneider et al. 2012; Peretto et al. 2013; Dewangan et al. 2015).

We also see diffuse and nebulous features at the apparent double centre in the HGBS 100 µm map (see Fig. 4). At 100 µm the emission is concentrated in the central part of the filament hub, at IRAS 05451+0037 and emission star LkHα 316, and features diffuse lobes and loops. This kind of activity at 100 µm (and also at 70 µm) cannot be found in the neighbourhood; at least within $\sim$17 arcmin to the south, and up to $\sim$1°.8 to the north, north-east (as far as L1622). For a better visualization of the central part of NGC 2071-N, at various wavelengths, see Section 4.3.

For the following calculations we mainly choose core positions, displayed in Fig. 3, left, that are sampling the filaments and the hub centre. Around them, we defined spots/circles (see Fig. 5) within which we then performed the measurements and calculations. For their sizes we defined a uniform 25 arcsec (i.e. $\sim$0.05 pc) radius, knowing that the median FWHM size of the HGBS cores in this subregion is 0.05 pc. We may take the FHWM size as a radius, because (1) the column density profile of a critical Bonnor–Ebert sphere (e.g. Bonnor 1956) with outer radius R_{BE} is very well approximated by a Gaussian profile of FWHM $\sim R_{BE}$ (see in Könyves et al. 2015), and (2) for a Gaussian 2D circular distribution, $\sim$94 per cent of the emission is contained within a circular aperture of radius FWHM (see also in Peretto, André & Belloche 2006). Thus, closely 100 per cent of the flux and mass of the cores is contained in the – preferably non-overlapping – drawn circles in Fig. 5, within which we can also sample the molecular emission with independent beams. The two circles #1 and #3 were placed over column density peaks, and the rest of the positions mostly correspond to starless, pre-stellar, protostellar dense cores, or YSOs. In these spheres we assume uniform densities.

3.3 Molecular line data

Low- and high-density molecular line tracers of gas kinematics were also analysed in our NGC 2071-North hub. ^{13}CO (1–0) and C^{18}O (1–0) observations were done with the IRAM 30-m telescope, HCN (1–0), H^{13}CN (1–0) and HCO^{+} (1–0), H^{13}CO^{+} (1–0) mapping were performed with the Nobeyama 45-m antenna.

Sample spectra of all these observed lines are displayed in Fig. 6. As example spot #7 has $A_V \sim 8$ mag, while the visual extinction is higher ($\sim$19 mag) in spot #23, which is also located at the junction of filaments in the central part of the hub. Among other properties, A_V values are listed for each analysis spot in Table 1. All of the averaged spectra over these spots, where available, are included in Appendix A. When we find a reasonable Gaussian fit of the main component of the line, it is also overplotted on the spectra. The goodness of the fits has been evaluated with residual sum of squares, then we also eye inspected the results.

Table 1. Physical properties of 42 selected locations within 25 arcsec radius in NGC 2071-N, shown in Fig. 5. See Sections 3.2 and 3.4 for details.

Spot no. (1)	RA$_{2000}$ ($^{\mathrm{h\ m\ s}}$) (2)	Dec.$_{2000}$ ($^{\circ\ \prime\ \prime\prime}$) (3)	A_V (mag) (4)	Mass (M$_\odot$) (5)	T_dust (K) (6)	$n^\mathrm{ave}_{\mathrm{H}_2}$ (10^4 cm^{-3}) (7)	u_grav (10^{-10} erg cm^{-3}) (8)	$\overline{P}_\mathrm{G}/k_\mathrm{B}$ (10^5 K cm^{-3}) (9)	Obj$_\mathrm{type}$ (10)
1	05:47:37.00	+00:38:10.3	17.7	2.75	13.4 ± 0.3	8.33	5.70	18.71	–
2	05:47:40.72	+00:38:16.4	12.7	2.06	13.3 ± 0.1	6.23	3.19	10.50	–
3	05:47:44.50	+00:38:22.2	28.7	4.34	13.4 ± 0.5	13.16	14.21	46.59	–
4	05:47:49.62	+00:38:22.9	14.2	2.18	12.8 ± 0.1	6.61	3.58	11.75	Pre-stellar core[1]
5	05:47:55.55	+00:38:22.1	8.6	1.28	13.6 ± 0.1	3.88	1.23	4.05	–
6	05:48:01.29	+00:37:53.8	8.2	1.29	13.7 ± 0.1	3.93	1.26	4.12	Pre-stellar core[1]
7	05:48:01.75	+00:36:38.9	8.2	1.28	13.5 ± 0.2	3.87	1.23	4.05	–
8	05:47:59.56	+00:35:34.3	12.9	1.91	14.1 ± 0.6	5.80	2.77	9.02	Protostellar core[1]
9	05:47:56.12	+00:33:33.7	6.5	1.02	14.0 ± 0.2	3.10	0.79	2.57	Pre-stellar core[1]
10	05:48:07.68	+00:33:49.9	13.6	2.46	13.1 ± 0.2	7.46	4.56	14.97	Protostellar core[1]
11	05:47:42.98	+00:37:19.6	16.7	2.45	13.0 ± 0.2	7.44	4.55	14.85	Pre-stellar core[1]
12	05:47:46.43	+00:36:39.6	17.3	2.68	12.6 ± 0.2	8.12	5.41	17.77	–
13	05:47:41.96	+00:36:10.2	18.5	2.81	12.4 ± 0.3	8.51	5.94	19.53	Pre-stellar core[1]
14	05:47:38.18	+00:35:57.0	13.2	2.05	12.9 ± 0.2	6.22	3.18	10.39	–
15	05:47:34.59	+00:35:42.3	19.0	2.98	12.4 ± 0.2	9.04	6.71	21.97	Pre-stellar core[1]
16	05:47:30.05	+00:35:21.4	12.1	1.89	13.0 ± 0.1	5.72	2.69	8.84	–
17	05:47:25.18	+00:35:06.8	24.8	3.97	11.7 ± 0.3	12.04	11.90	38.98	Pre-stellar core[1]
18	05:47:05.91	+00:35:31.3	6.6	1.01	14.1 ± 0.2	3.07	0.77	2.52	Starless core[1]
19	05:47:40.36	+00:39:07.4	9.5	1.50	13.5 ± 0.1	4.54	1.69	5.57	–
20	05:47:43.73	+00:39:26.2	12.1	1.82	13.5 ± 0.3	5.53	2.51	8.19	–
21	05:47:35.51	+00:39:04.8	13.6	2.11	14.1 ± 0.3	6.40	3.36	11.01	Pre-stellar core[1]
22	05:47:37.46	+00:39:34.5	18.8	2.98	13.2 ± 0.4	9.03	6.69	21.97	Pre-stellar core[1]
23	05:47:40.82	+00:40:11.5	18.6	3.11	12.5 ± 0.3	9.43	7.30	23.92	Pre-stellar core[1]
24	05:47:42.97	+00:40:57.4	12.0	1.86	13.3 ± 0.1	5.65	2.62	8.56	YSO[2,4]
25	05:47:46.66	+00:41:00.7	12.9	2.04	13.3 ± 0.1	6.18	3.14	10.29	Pre-stellar core[1]
26	05:47:49.30	+00:41:45.7	9.4	1.44	13.6 ± 0.1	4.38	1.57	5.13	Pre-stellar core[1]
27	05:47:53.00	+00:41:55.3	6.3	0.98	14.1 ± 0.1	2.98	0.73	2.38	–
28	05:47:56.80	+00:42:00.1	5.9	0.90	14.2 ± 0.1	2.73	0.61	2.00	Dense core[3]
29	05:48:03.10	+00:42:01.1	5.1	0.79	14.4 ± 0.1	2.39	0.47	1.54	Pre-stellar core[1]
30	05:47:47.61	+00:43:32.8	9.6	1.48	13.4 ± 0.1	4.49	1.66	5.42	Pre-stellar core[1]
31	05:47:56.03	+00:44:32.0	9.2	1.38	13.6 ± 0.1	4.19	1.44	4.71	Pre-stellar core[1]
32	05:47:51.61	+00:45:51.3	6.8	1.07	14.2 ± 0.1	3.24	0.86	2.83	Starless core[1]
33	05:47:58.87	+00:46:25.0	8.5	1.31	13.9 ± 0.1	3.97	1.29	4.24	Pre-stellar core[1]
34	05:47:34.40	+00:39:59.1	15.0	2.31	13.2 ± 0.1	7.02	4.04	13.2	YSO[2,5]
35	05:47:31.17	+00:40:00.3	16.0	2.58	13.0 ± 0.2	7.81	5.01	16.46	Pre-stellar core[1]
36	05:47:34.97	+00:41:30.5	14.7	2.39	12.9 ± 0.2	7.23	4.30	14.13	Pre-stellar core[1]
37	05:47:28.00	+00:41:03.1	13.0	2.12	13.2 ± 0.2	6.42	3.38	11.12	Dense core[3]
38	05:47:28.14	+00:42:01.1	10.9	1.66	13.5 ± 0.1	5.03	2.07	6.82	Pre-stellar core[1]
39	05:47:24.34	+00:42:31.9	11.3	1.73	13.5 ± 0.1	5.26	2.27	7.40	–
40	05:47:20.45	+00:42:59.5	16.0	2.50	13.1 ± 0.1	7.58	4.72	15.46	Pre-stellar core[1]
41	05:47:15.96	+00:42:17.6	16.0	2.55	13.2 ± 0.1	7.74	4.91	16.08	Pre-stellar core[1]
42	05:47:23.24	+00:44:18.0	17.5	2.69	12.9 ± 0.1	8.16	5.46	17.90	Pre-stellar core[1]

Note. Columns: (1): spot numbers, as in Fig. 5; (2) and (3): right ascension and declination of spot centres; (4): visual extinction calculated from median column density assuming N_{H_2} (cm^{-2}) = 0.94 × 10^{21} A_V (mag) (Bohlin, Savage & Drake 1978); (5): dust mass within these circles, no 20 per cent error is included; (6): dust temperature with standard deviation uncertainty; (7): average volume density; (8): gravitational energy density; (9): volume-averaged gravitational pressure; (10): type of central object taken from the following studies: [1]Könyves et al. (2020); [2]Megeath et al. (2012); [3]Kirk et al. (2016); [4]Gaia Collaboration et al. (2018); and [5]Cutri et al. (2003).

Given the high column density values across NGC 2071-N, we first evaluated the optical depth of the HCO$^+$ and HCN lines with the help of their ^{13}C isotopes. We considered the same assumptions as Shimajiri et al. (2017) and used their equation (8) for deriving τ^{HCO^+} and τ^{HCN}. The peak intensity of the rare isotopic species we could fit only in limited cases (see Fig. A2 for H^{13}CO$^+$ (1–0), and Fig. A3 for H^{13}CN (1–0)). At the velocity position of the peak of the fit, we recorded the observed intensity (in T_MB) of the averaged H^{13}CO$^+$ and H^{13}CN lines, then that of the main species, HCO$^+$ and HCN, at the same position. The resulting optical depths are listed in Table 2. The actual number results suggest that the HCO$^+$ and HCN lines are optically thick, however $\tau^{\mathrm{HCO}+}$ at circle #8, and τ^{HCN} at spot #24 may be upper limits. At the locations where the intensity of the main species is weaker than that of the rare species, most probably due to self-absorption, we indicate ≫1 as optical depth. In the rest of the cases, the emission of the rare species was not detected, or not well characterized by the fit. At the same time, based on the spectra, however noisy, we assume that the rare species, H^{13}CO$^+$ and H^{13}CN, remain optically thin, or nearly so. Considering the critical densities of these rare J = 1 → 0 lines at 10 K for local thermodynamic equilibrium (LTE), that is $n_{\mathrm{crit}}^{\mathrm{H^{13}CO^+}} = 1.5 \times 10^5$ cm^{-3} and $n_{\mathrm{crit}}^{\mathrm{H^{13}CN}} = 2.0 \times 10^6$ cm^{-3} (Dhabal et al. 2018), our estimated volume densities are everywhere lower (see Table 1), with a median value of 6.23 × 10^4 cm^{-3}.

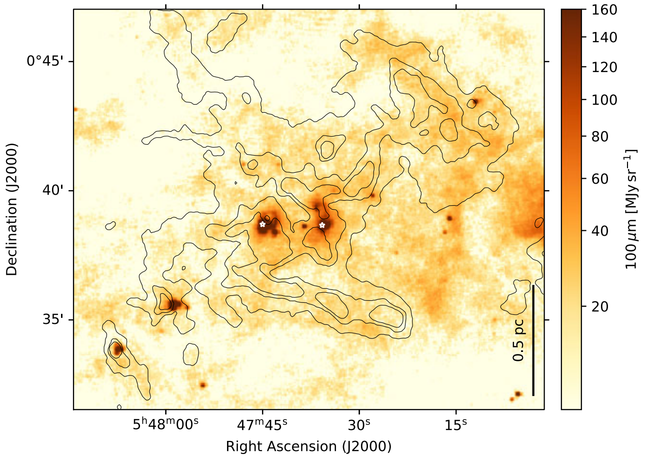

Figure 4. The same region as above in 100 μm emission. The left- and right-hand white stars mark the locations of IRAS 05451+0037 and LkHα 316, respectively.

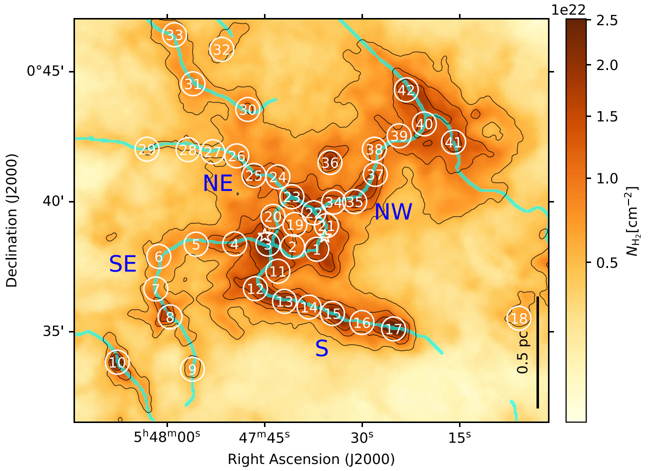

Figure 5. Column density map and filaments in NGC 2071-N, as in Fig. 3, left. White numbered circles with 25 arcsec radius indicate the spots within which we estimated the energy balance (see Sections 3.4 and 4.2, and Tables 1 and 2). Filament designations by their locations are also shown: southern (S); south-east (SE); north-east (NE); and north-west (NW).

High-density molecular tracers, especially when combining an optically thick and a thin line, can also indicate infalling gas, and thus global collapse of parts of the cloud (e.g. Myers et al. 1996; Evans 1999; Schneider et al. 2010; Rygl et al. 2013; He et al. 2015; Traficante et al. 2017). This shows up in the thick tracer (i.e. HCO^+) as a blue–red asymmetry, with brighter blueshifted peak, whereas the thin line ($H^{13}CO^+$) peaks at the velocity of the self-absorption dip. Such configuration of the thin and thick lines we find in a couple of positions along the filaments (see Fig. A2) that we note with a superscript 'c' in column (5) of Table 2. At these spots we have a strong hint that self-gravity plays a significant role that further analysis may confirm (see Sections 3.4 and 4.2). These locations, except one, lie along the southern filament. Profiles of this shape also provide confirmation that the thick double peaks are not coming from two velocity components along the line of sight. Among these, the peaks of the thin lines (and the dips of the thick ones) are found at $V_{LSR} \sim 9$ km s^{-1}.

In addition to the presented line profiles and calculations, we are also providing the integrated intensity (moment 0) maps of the observed molecules in Appendix B, however they may be somewhat influenced by the optically thick conditions. In the case of the thin lines ($H^{13}CO^+$ and $H^{13}CN$), the integrated intensity of this region is much weaker and rather sparse.

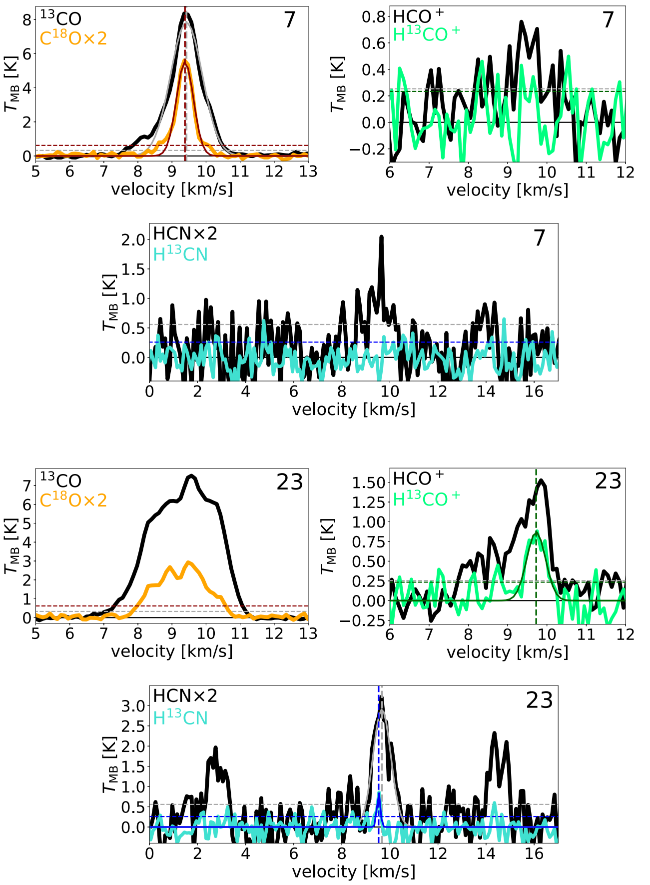

Figure 6. Spectra averaged over circles #7 and #23. All of them are J = 1 → 0 transitions. When it is reasonable, a Gaussian fit and its peak position are also included. Dashed horizontal lines mark rms thresholds; grey for the black spectra, in colour for the overplotted spectra (6σ rms level is indicated for the CO species, 3σ for the HCX species). All of the averaged spectra over the analysis circles (see Fig. 5) are included in Appendix A, when available. Derived properties from these molecular lines are listed in Table 2.

3.4 Energy balance in NGC 2071-North

From column density and optically thin molecular line data we have estimated gravitational and turbulent kinetic energy densities, as well as related gravitational and internal pressures in several spots within the region. These pressure terms contribute to the energy densities, nevertheless they are often equivalently used to evaluate the stability of clumps and clouds. We will separately probe the interplay between gravity and turbulence with the energy density and pressure properties, estimated with standard formulas and assumptions.

Throughout the calculations we assume that the cores have spherical shape, uniform density, no contribution of external pressure or support of magnetic field, and no rotation either. In NGC 2071-N there are no available polarization observations (with comparable resolution to the above data) that we could derive magnetic energy densities, therefore we did not attempt to derive it from *Planck* measurements on 5 arcmin scale, which would most probably characterize different phenomena.

Table 2. Physical properties of 42 selected locations within 25 arcsec radius in NGC 2071-N, shown in Fig. 5. See Sections 3.3 and 3.4 for details.

	^{13}CO	C^{18}O	HCO$^+$		H^{13}CO$^+$			HCN		H^{13}CN		
Spot # (1)	$\sigma_{\rm NT}^{\rm ^{13}CO}$ (km s^{-1}) (2)	$\sigma_{\rm NT}^{\rm C^{18}O}$ (km s^{-1}) (3)	$\sigma_{\rm NT}^{\rm HCO^+}$ (km s^{-1}) (4)	$\tau^{\rm HCO+}$ – (5)	$\sigma_{\rm NT}^{\rm H^{13}CO^+}$ (km s^{-1}) (6)	$u_{\rm turb}^{\rm H^{13}CO^+}$ (10^{-10} erg cm^{-3}) (7)	$P_{\rm int}^{\rm H^{13}CO^+}/k_{\rm B}$ (10^5 K cm^{-3}) (8)	$\sigma_{\rm NT}^{\rm HCN}$ (km s^{-1}) (9)	$\tau^{\rm HCN}$ – (10)	$\sigma_{\rm NT}^{\rm H^{13}CN}$ (km s^{-1}) (11)	$u_{\rm turb}^{\rm H^{13}CN}$ (10^{-10} erg cm^{-3}) (12)	$P_{\rm int}^{\rm H^{13}CN}/k_{\rm B}$ (10^5 K cm^{-3}) (13)
1	–	–	0.48 ± 0.03	11	0.19 ± 0.07	2.09 ± 1.91	3.38 ± 3.10	–	–	–	–	–
2	–	–	–	–	–	–	–	–	–	–	–	–
3	–	–	–	$\gg$1	0.39 ± 0.05	14.32 ± 6.47	24.38 ± 11.02	–	–	–	–	–
4	–	–	–	–	–	–	–	–	–	–	–	–
5	–	–	–	–	–	–	–	–	–	–	–	–
6	0.60 ± 0.01	0.39 ± 0.01	–	–	–	–	–	–	–	–	–	–
7	0.47 ± 0.01	0.24 ± 0.01	–	–	–	–	–	–	–	–	–	–
8	0.43 ± 0.02	0.27 ± 0.01	–	90	0.33 ± 0.07	4.52 ± 2.92	7.64 ± 4.93	0.54 ± 0.08	–	–	–	–
9	0.31 ± 0.01	0.18 ± 0.01	–	–	–	–	–	–	–	–	–	–
10	–	–	–	–	–	–	–	–	–	–	–	–
11	–	–	–	–	–	–	–	–	–	–	–	–
12	–	–	–	$\gg$1$^{\rm c}$	0.24 ± 0.05	3.21 ± 2.01	5.33 ± 3.34	–	–	–	–	–
13	–	–	–	$\gg$1$^{\rm c}$	0.23 ± 0.04	3.09 ± 1.60	5.12 ± 2.66	–	–	–	–	–
14	–	–	–	$\gg$1$^{\rm c}$	0.21 ± 0.05	1.88 ± 1.28	3.08 ± 2.10	–	–	–	–	–
15	–	–	–	$\gg$1$^{\rm c}$	0.22 ± 0.06	3.09 ± 2.21	5.11 ± 3.66	–	–	–	–	–
16	–	–	–	$\gg$1$^{\rm c}$	0.21 ± 0.05	1.77 ± 1.20	2.91 ± 1.97	–	–	–	–	–
17	–	–	–	$\gg$1$^{\rm c}$	0.24 ± 0.04	5.05 ± 2.72	8.45 ± 4.55	0.23 ± 0.03	–	–	–	–
18	–	–	–	–	–	–	–	–	–	–	–	–
19	–	–	–	–	–	–	–	–	–	–	–	–
20	–	–	–	–	–	–	–	–	–	–	–	–
21	–	–	0.43 ± 0.02	–	–	–	–	–	–	–	–	–
22	–	–	–	14	0.26 ± 0.06	4.23 ± 2.97	7.07 ± 4.97	–	–	–	–	–
23	–	–	–	59	0.24 ± 0.04	3.76 ± 2.02	6.27 ± 3.36	0.37 ± 0.04	61	0.07 ± 0.02	0.29 ± 0.23	0.25 ± 0.20
24	–	–	–	–	–	–	–	–	89	0.11 ± 0.06	0.46 ± 0.45	0.64 ± 0.60
25	0.77 ± 0.02	0.39 ± 0.01	–	–	–	–	–	–	–	–	–	–
26	0.66 ± 0.01	0.31 ± 0.01	–	–	–	–	–	–	–	–	–	–
27	0.65 ± 0.02	0.27 ± 0.01	–	–	–	–	–	–	–	–	–	–
28	–	–	–	–	–	–	–	–	–	–	–	–
29	–	–	–	–	–	–	–	–	–	–	–	–
30	–	–	–	–	–	–	–	–	–	–	–	–
31	–	–	–	–	–	–	–	–	–	–	–	–
32	–	–	–	–	–	–	–	–	–	–	–	–
33	–	–	–	–	–	–	–	–	–	–	–	–
34	–	–	–	30	0.19 ± 0.06	1.73 ± 1.48	2.81 ± 2.40	–	–	–	–	–
35	–	–	–	34	0.19 ± 0.07	2.03 ± 1.86	3.30 ± 3.03	–	–	–	–	–
36	–	–	–	$\gg$1	0.11 ± 0.03	0.62 ± 0.42	0.88 ± 0.60	–	–	–	–	–
37	–	–	–	–	–	–	–	–	–	–	–	–
38	–	–	–	$\gg$1	0.08 ± 0.03	0.23 ± 0.22	0.26 ± 0.24	–	–	–	–	–
39	–	–	–	$\gg$1$^{\rm c}$	0.05 ± 0.03	0.11 ± 0.10	0.05 ± 0.04	–	–	–	–	–
40	–	–	–	–	–	–	–	–	–	–	–	–
41	–	–	–	–	–	–	–	–	–	–	–	–
42	–	–	–	–	–	–	–	–	–	–	–	–

Note. Columns: (1): spot numbers, as in Fig. 5; (2), (3), (4), (6), (9), (11): non-thermal velocity dispersion and uncertainties of the given (1–0) lines, ^{13}CO, C^{18}O, HCO$^+$, H^{13}CO$^+$, HCN, H^{13}CN, respectively; (5) and (10): optical depth of HCO$^+$ and HCN, respectively; (7) and (12): turbulent kinetic energy densities and errors from H^{13}CO$^+$ and H^{13}CN linewidths, respectively; (8) and (13): internal pressure and uncertainties at the latter locations. A superscript ‘c’ in column (5) marks the spots where HCO$^+$ spectra show infall signatures (see Fig. A2).

The gravitational energy density was estimated from $u_{\rm grav} = 4/5\pi G\rho^2 R^2$ (see e.g. Lyo et al. 2021), where G is the gravitational constant, and $\rho = \mu m_{\rm H} n_{\rm H_2}$ is the uniform density for which the volume density we calculated from the *Herschel* column density map of Könyves et al. (2020) (column 7 of Table 1). R is the sphere radius (25 arcsec), $\mu = 2.8$ is the mean molecular weight per H_2 molecule, and $m_{\rm H}$ is the hydrogen atom mass.

These calculations gave a mean value of $u_{\rm grav} = 3.6 \times 10^{-10}$ erg cm^{-3} with a standard deviation of 2.8×10^{-10} erg cm^{-3}, for the whole range of results at the 42 locations in Fig. 5.

For a later comparison, the volume-averaged gravitational pressure can be estimated as $\overline{P}_{\rm G}/k_{\rm B} \approx 1.01 a_1 \langle \phi_{\rm G} \rangle M^2 R^{-4}$, expressed by Bertoldi & McKee (1992), and used, for example, by Sadavoy et al. (2015). $k_{\rm B}$ is the Boltzmann constant, $a_1 = 1.3$ is a scaling factor that measures the effects of a non-uniform density distribution; our value is appropriate for a self-gravitating cloud. $\phi_{\rm G}$ is a scaling factor describing the cloud geometry; we consider $\phi_{\rm G} = 1$ for perfect spheres. M (in $M_\odot$) is the mass of the clumps (column 5 of Table 1), $R = 0.048$ pc (used in pc) is the radius of our spots/spheres. We thus calculated the volume-averaged gravitational pressures that give a mean value of $\overline{P}_{\rm G}/k_{\rm B} = 11.8 \times 10^5$ K cm^{-3} and a standard deviation of 9.3×10^5 K cm^{-3} for the whole range of results.

The individual values are listed in Table 1, along with additional physical properties. We assumed 20 per cent error on the column densities, mass, then on the volume densities, energy densities, and pressures in order to avoid the propagation of the typical factor of about 2 systematic errors mainly due to the uncertainties in the dust opacity law.

The turbulent kinetic energy densities were calculated from $u_{\rm turb} = 3/2\rho\sigma_{\rm NT}^2$, where $\sigma_{\rm NT}$ is the non-thermal component of the velocity dispersion. For this, first we converted the linewidths, as $\sigma = \Delta v/\sqrt{8\ln 2}$, that we estimated by Gaussian fitting to the observed profiles of $H^{13}CO^+$ (1–0) and $H^{13}CN$ (1–0), where it was possible (see Section 3.3). Then, we separated the non-thermal component $\sigma_{\rm NT}$ using a similar relation to equation (6) of Dunham et al. (2011), and found that the observed velocity dispersions (or linewidths) are almost entirely due to non-thermal motions. These, we assume, may represent random turbulent motions (and infall motions), which are independent of the gas temperature. The resulting turbulent kinetic energy densities (for $H^{13}CO^+$, where it was possible to derive) yield a mean of $u_{\rm turb}^{\rm H^{13}CO^+} = 3.23 \times 10^{-10}$ erg cm^{-3} with a high standard deviation of 3.20×10^{-10} erg cm^{-3}. From $H^{13}CN$ data, we could calculate $u_{\rm turb}^{\rm H^{13}CN}$ only in two cases. See Figs A2 and A3 for the fitted line profiles, and Table 2 for the derived line properties.

In comparison to the gravitational pressure, we estimate the internal pressure as well in the spots, where the quality of the $H^{13}CO^+$ (1–0) and $H^{13}CN$ (1–0) spectra allowed us to derive turbulent kinetic energy densities too. The internal pressure can be approximated from the ideal gas law, as $P_{\rm int}/k_{\rm B} \approx n_{\rm H_2}^{\rm ave}\sigma_{\rm NT}^2$, where $n_{\rm H_2}^{\rm ave}$ is the average volume density (column 7 of Table 1), and $\sigma_{\rm NT}$ is the non-thermal part of the velocity dispersion, as above. In this or similar form the internal pressure has been calculated, for example, by Hatchell et al. (2005), Sadavoy et al. (2015), Pattle et al. (2015), and Miville-Deschênes, Murray & Lee (2017). The gravitational pressure estimates from $H^{13}CO^+$ can be summarized with a mean value of $P_{\rm int}/k_{\rm B} = 5.4 \times 10^5$ K cm^{-3} with an as large standard deviation of 5.4×10^5 K cm^{-3}.

Apart from the 20 per cent uncertainties inherited from the column density measurements, we consider 1 standard deviation uncertainties on the measured median dust temperatures within the sampling spots. Along with the calculations of $\sigma_{\rm NT}$, $u_{\rm turb}$, and $P_{\rm int}$ we propagated the corresponding individual errors using the maximum error formula (see Tables 1 and 2, and Fig. 7 for the visualization of the uncertainties).

The left-hand panel of Fig. 7 shows the estimated energy densities, where both $u_{\rm grav}$ and $u_{\rm turb}$ (latter from $H^{13}CO^+$ or $H^{13}CN$) could be calculated. Such spots are denoted on the horizontal axis. In the right-hand panel of Fig. 7, black and red data points display the volume-averaged gravitational pressure and internal pressure of these same locations, respectively, using the same molecular lines as in the left-hand panel. In both panels yellow stars indicate the positions where we observed possible infall signatures based on the blue–red asymmetry of the averaged HCO^+ profiles (see Fig. A2). For a discussion involving Fig. 7, see Section 4.2.

4 DISCUSSION

4.1 Large-scale magnetic field pattern

Revisiting the panels of Fig. 1, we can see the large-scale structure of the plane-of-sky (POS) magnetic field that was discussed in Soler (2019) for the whole Orion A and B clouds. What shows up in Fig. 1 right is that the POS magnetic field (on the scale of 1/3 of the 5 arcmin *Planck* beam) is largely horizontal in the eastern part, and vertical in the western part, as it would turn and change orientation across the hub.

Comparing Fig. 1, left, with fig. 4 of Soler (2019) and fig. 8 of Tahani et al. (2018), we can see that there is a magnetic loop structure apparently starting or ending at NGC 2071, extending up to NGC 2071-N, while the *B*-field lines run mostly along the right ascension lines in the western side of all the clouds shown in Fig. 1, left.

Providing that the magnetic field is carrying material, a significant change in the *B*-field orientation (i.e. from horizontal to perpendicular) may be an efficient configuration for deposing and gathering gas and dust, which could also explain the location of this relatively small and isolated cloud. Not discussing here other physical forces, indeed it can be seen in the ISM that the *B* field shows a bend and turns at high-density (elongated) molecular clouds, such as Orion A, Perseus, unlike in Musca and the Chamaeleon, for example. See these maps of *Planck* POS magnetic field and column density in Soler (2019).

We note that in the case of Orion A, such a simple visualization helped Tahani et al. (2018) to conclude that a bow-shaped magnetic field is surrounding that filament.

However, how the large-scale magnetic field is cascading down, and most likely affecting the morphology of the centre of the hub, is not yet known.

4.2 Coherent structure with contracting cores

Gibb (2008) has noticed that NGC 2071-N attracted very little study since the 1980s (Fukui et al. 1986; Iwata et al. 1988), which continues to hold ever since 2008. It is located at ∼20 arcmin north of the NGC 2071 reflection nebula, and its structures turned out to be more extended than the 0.7 pc diameter clump first seen in $C^{18}O$ (Iwata et al. 1988). While NGC 2071-N seems isolated from the rest of the L1630-North complex at the H_2 column density level of $\sim 1 \times 10^{22}$ cm^{-2}, it is well part of it within the contours at $\sim 2 \times 10^{21}$ cm^{-2}. At this higher value, NGC 2071-N looks more fragmented than, for example, the region of HH 24–26, south of the NGC 2068 reflection nebula (see Fig. 1, left, at RA ∼ $05^{\rm h}46^{\rm m}$, Dec. ∼ –00°15′). As we go down from this higher to the lower value, the column density contours become more extended around NGC 2071-N, than around

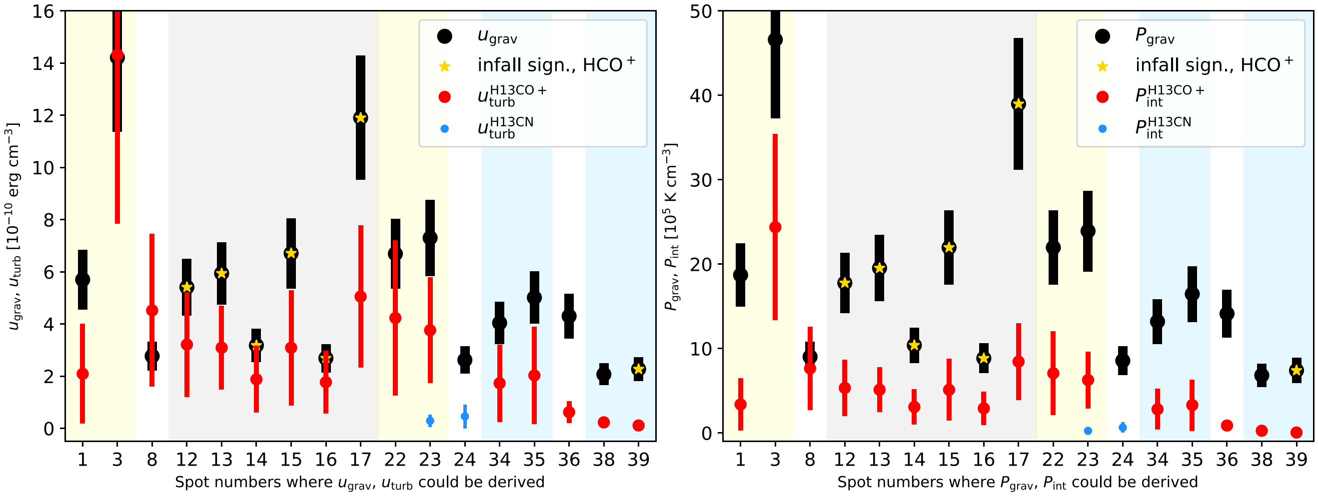

Figure 7. Left: gravitational and turbulent energy densities (in 10^{-10} erg cm^{-3}) with uncertainties. Right: volume-averaged gravitational pressure and internal pressure (in 10^5 K cm^{-3}), more precisely in the form of $P/k_{\rm B}$. They are indicated per spot number, where both pairs could be calculated; see the legends. The yellow stars mark the positions where the blue–red asymmetry of HCO$^+$ lines revealed possible infall signatures. See Tables 1 and 2 for details, and Fig. 5 for the numbered analysis spots. Among the latters, light yellow background marks the spots that are along the central filament loop. Light grey background shows the spots in the southern filament, and light blue background indicates the ones along the north-western filament. See Sections 3.4 and 4.2 for details.

HH 24–26. In other words, the same mass lies in a somewhat larger area in NGC 2071-N. The high column density fragments in our subregion are the two centres, portions of surrounding filaments, and the extension at the north-west (see e.g. Fig. 1, right). The basis of this simple comparison is the similar projected location of both subregions, i.e. north/south of a reflection nebula, respectively, on either side of the L1630-North complex (see Fig. 1, left). The above may mean that NGC 2071-N still has a great potential to form more solar-type stars over a longer period of time.

At the time of Iwata et al. (1988), on the other hand, they inferred that this cloud is nearly in dynamical equilibrium, having calculated the same figures both for the gravitational energy and for total kinetic energy of internal turbulence. Then, Goldsmith et al. (1992) found their C^{18}O clumps gravitationally unbound and deemed as probably transient structures.

We infer the current activity of this cloud from Fig. 7, the left-hand panel of which shows that the gravitational energy densities dominate over the turbulent kinetic energy densities in most of the displayed positions. This same trend is also supported by the right-hand panel of Fig. 7, that is that the volume-averaged gravitational pressures are higher than the internal turbulent pressures.

In spot #8, at the dense tip of the south-east filament, the energy balance is less conclusive. Here, we measure one of the largest velocity dispersions based on the H^{13}CO$^+$ and HCN lines; $\sigma_{\rm NT}^{\rm H^{13}CO^+}$ is larger than that of the large-scale C^{18}O, and $\sigma_{\rm NT}^{\rm HCN}$ is even larger than $\sigma_{\rm NT}^{\rm ^{13}CO}$. However, the velocity dispersions of H^{13}CO$^+$ and HCN at spot #8 are fairly noisy that probably led to their overestimations, and therefore to higher turbulent energy densities and internal pressures.

Among the clumps along the central hub ring, in particular #3 (around IRAS 05451+0037), #22, #23 that are located at junctions of filaments, we also observe higher estimated $u_{\rm turb}^{\rm H^{13}CO^+}$ and $P_{\rm int}^{\rm H^{13}CO^+}$ (Fig. 7). Besides the noisy lines, this might also arise from infalling material along the filaments, however more investigations on this are out of the scope of this paper.

In addition to the marked HCO$^+$ infall candidates in Fig. 7, we can also identify blueshifted asymmetric line profiles in the optically thick C^{18}O (Fig. A1), in more than the already marked positions. Together with the indications that inside-out collapse has been detected in these clumps (Evans 1999), the overall higher gravitational energy densities and pressures support the picture that gravity is acting stronger on spatial scales of ∼0.05 pc and is currently forming new stars in several spots of this region.

4.3 Hub with a double centre

The HGBS column density map shows a detailed filamentary structure, both at $A_{\rm V} \sim 5$ and 10 mag contours (see Fig. 3, left), which was not known before. We suggest that a double centre may be formed in this hub, because the converging locations of the filaments south and south-east, and north-east and north-west are somewhat offset along the hub ring that is traced by a filament loop. In other words, the converging locations of filament pairs are offset. This offset is about 2.3 arcmin (0.27 pc) measured from spot #3 to #22, (see Fig. 5), while there is almost the same projected distance between the *IRAS* and LkHα sources. Circle positions #3 and #22 correspond to the ammonia cores D and C, respectively, defined by Iwata et al. (1988), while #3 contains IRAS 05451+0037 too. This span also matches the diameter of a ring-like structure that can be approximated from the combined emission at HCO$^+$ and HCN (Fig. B1), given that the maxima of their integrated intensities are scattered along the hub ring. This ring may indicate a transition and the connection between the hub and the filaments. We note that the junction of filament north-east and that of filament north-west with the hub ring are not appearing as one projected point (as apparently the junction of filaments south and south-east on the central ring), however the western section of the hub ring, ∼0.1 pc around the nominal position of core C along the filaments, seems to be an active spot of star formation with dense cores and protostars (see Fig. 3, left).

Hub–filament systems are expected to feature one single centre on a larger scale, while they may break up after a closer look. Based on molecular line data, Treviño-Morales et al. (2019) extracted a complex filamentary network in Monoceros R2 (Mon R2; $d \sim 830$ pc) also with a ring at the hub centre, where radially oriented filaments are joining from larger scales (see their fig. 4). Their hub ring has a radius of approximately 0.30 pc that we read from their figures, while that of ours is ∼0.13 pc that was estimated from a fitted circle

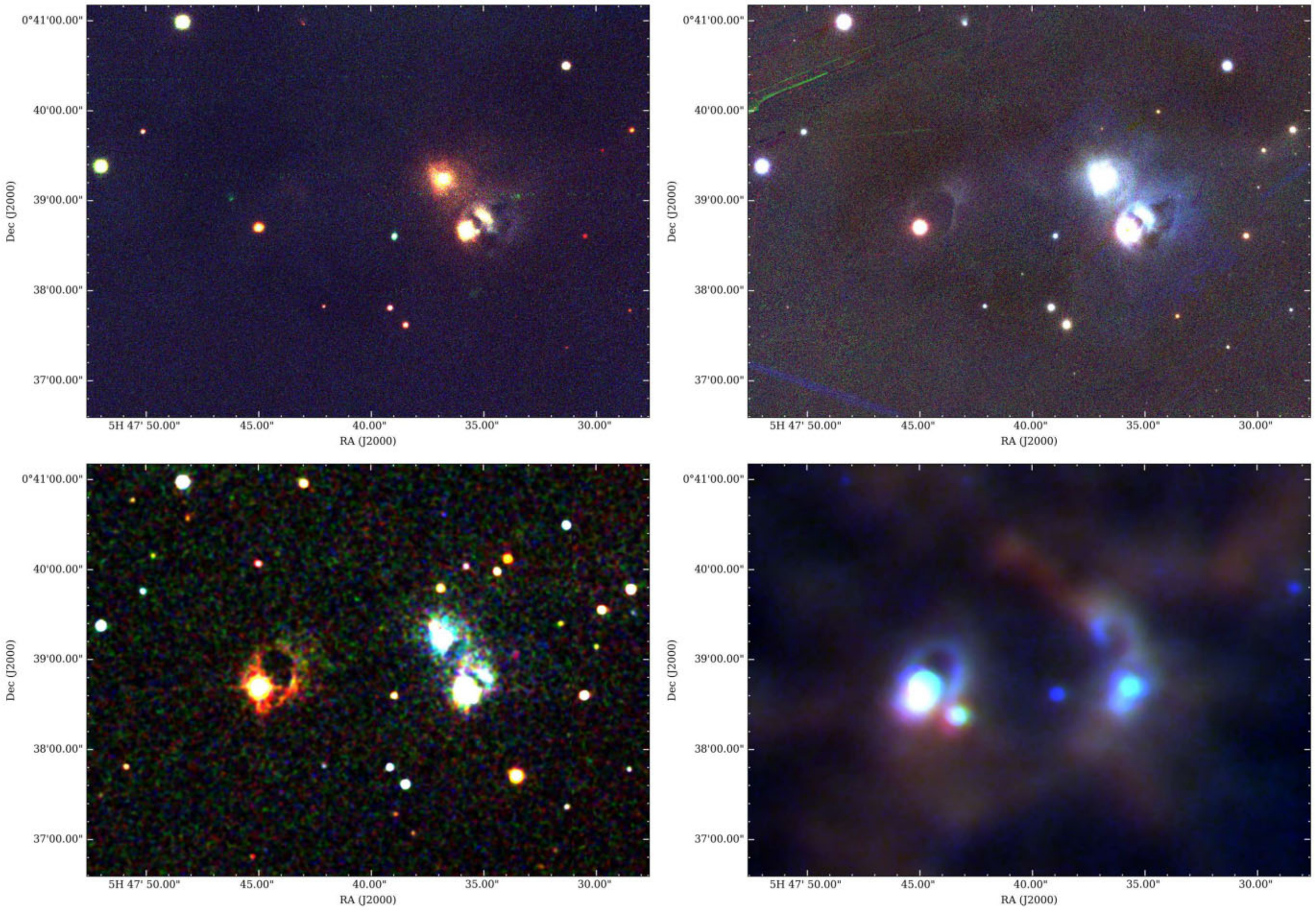

Figure 8. Zoomed RGB images on the double centre of the NGC 2071-N filament hub. The left-hand side source, mid-plane, is IRAS 05451+0037 and the lower right-hand side one is LkHα 316. Top-left: SDSS *i*, *r*, *g* images (in the RGB order). Top-right: Pan-STARRS *y*, *z*, *i* filters. Bottom-left: 2MASS K_s, *H*, *J* filters. Bottom-right: *Herschel* 250, 160, and 100 μm images. All listed in the RGB order, while Table 3 lists the nominal wavelengths of all these filters and images from the shortest to the longest wavelengths.

to the closed loop of filament skeletons. There is a massive cluster forming in the Mon R2 filament hub (Rayner et al. 2017), unlike in NGC 2071-N. Its most massive star IRS 1 ($\sim$12 M$_\odot$) appears close in projection to the location where multiple filaments arrive onto the Mon R2 hub ring. IRS 1 is also associated with an ultra-compact H II region that may have helped clean the innermost ring area of the ^{13}CO and C^{18}O emission, while our hub centre is not devoid of the large-scale emission (see Fig. B1).

Their central hub (without the extending filament arms) has a radius of $\sim$1 pc within which the mass is about 1000 M$_\odot$, and the visual extinction is much higher than in NGC 2071-N, above $\sim$20 mag, also derived from *Herschel* observations (Rayner et al. 2017). The latter authors suggest that star formation is an ongoing process in the Mon R2 hub that has already been regulated by feedback, which is again a substantial difference between our subregions. However, probably more such central hub ring structures may exist on a larger scale of cloud properties.

4.4 At the centre of the hub

The sources in the central part of the hub, while it was not known that it is a hub, have been discussed in more detail by Aspin & Reipurth (2000) and Hillenbrand et al. (2012).

As it was mentioned before that this region is somewhat isolated, there are no such compact sources with nebulous emission in the vicinity either, which strengthens the confidence that IRAS 05451+0037 and LkHα 316 belong to the same neighbourhood (see also Section 3.1).

We have looked for these sources in archival data sets, and visualized the hub centre with a series of RGB images.[9] In Fig. 8, the left-hand side source is IRAS 05451+0037 and the lower right-hand side one is LkHα 316. The used surveys and their wavelengths are listed in Table 3.

We note that throughout the paper we are using the position of IRAS 05451+0037 given by SIMBAD, which is referring to Gaia Collaboration et al. (2018). This is almost identical to the one used by Hillenbrand et al. (2012) based on the associated SDSS source, but different from the position of this same *IRAS* source given by Wouterloot, Walmsley & Henkel (1988), Claussen et al. (1996), and Aspin & Reipurth (2000). The location of the latter authors is $\sim$40 arcsec west of ours, and the disagreement is most likely due to the large beam sizes of *IRAS*.

Aspin & Reipurth (2000) have identified new HH objects near compact reflection nebulae – that is our double centre in Fig. 8.

---

[9] Images were generated with the PYTHON package MULTICOLORFITS: https://github.com/pjcigan/multicolorfits

Table 3. Summary of surveys and wavelengths providing images for Fig. 8. SDSS: Eisenstein et al. (2011); Pan-STARRS: Chambers et al. (2016); 2MASS: Skrutskie et al. (2006); *Herschel*: Pilbratt et al. (2010).

Figure panel	Fig. 8, top-left			Fig. 8, top-right			Fig. 8, bottom-left			Fig. 8, bottom-right		
Survey	SDSS *g*	SDSS *r*	SDSS *i*	Pan-STR *i*	Pan-STR *z*	Pan-STR *y*	2MASS *J*	2MASS *H*	2MASS K_s	*Herschel* 100	*Herschel* 160	*Herschel* 250
Wavelength (µm)	0.4686	0.6165	0.7481	0.7520	0.8660	0.9620	1.24	1.66	2.16	100	160	250

Their HH 471 A–E jets and flows are associated with LkH*α* 316, and the earlier known HH 71 may as well, while HH 473–474 may be associated with the *IRAS* source as most likely exciting source. The new HH 472 seems to be associated with a faint and unknown source whose positions are identified by SIMBAD as 2MASS J05473897+0038362. Aspin & Reipurth (2000) suggested that this unknown exciting source of HH 472 may be responsible for driving the outflow found by Fukui et al. (1986) and Iwata et al. (1988); see Section 4.5.

The right-hand side group of reflection nebulosities also appear in the *I*-band images of Aspin & Reipurth (2000). LkH*α* 316 is the lowest compact source, LkH*α* 316-neb lies ∼15 arcsec north-west of it, and the 316/c component is the one ∼37 arcsec north-east of them. LkH*α* 316-neb is only a nebulosity without a star. Most probably LkH*α* 316 and LkH*α* 316-neb are physically associated (Aspin & Reipurth 2000), but we suggest that even 316/c may be part of this close system, visually based on the morphology of the diffuse gas and the curved material bridge that is best seen in the 2MASS and *Herschel* images (lower panels of Fig. 8).

Furthermore, another argument strengthening the physical association between all of the three LkH*α* 316 components is their locations in the column density map (see the contours in Fig. 4). The northern nebulosity is within the ammonia core C, at the junction of two filaments that can also be seen in the lower right-hand panel of Fig. 8. Summarized in Section 3.2, at such locations material is deposited from which YSOs and infrared clusters may form more efficiently, which can be further channelled in between 316/c and the two other nebulosities. The integrated intensity map of HCO^+ (1–0) in Fig. B1, also suggests a connection between LkH*α* 316 and LkH*α* 316-neb, both being on the island of strongest emission. IRAS 05451+0037 is also found at the junction of filaments within ammonia core D, which was originally found to drive a bipolar CO outflow (Fukui et al. 1986; Iwata et al. 1988). Hillenbrand et al. (2012) derived a bolometric luminosity of $\sim 90\,L_\odot$ for IRAS 05451+0037, and presented for the first time its optical SDSS spectrum as well. From the analysis from SDSS up to the James Clerk Maxwell Telescope (JCMT)/Submillimetre Common-User Bolometer Array (SCUBA) wavelengths and models, they concluded that IRAS 05451+0037 is optically faint and far-infrared bright, and its spectral energy distribution (SED) is consistent with those of Class I and flat-spectrum YSOs. They suggest that there is still likely a significant circumstellar envelope that is feeding the extended massive disc.

They found that our *IRAS* source is the brightest in the region at mid-infrared wavelengths based on the *Wide-field Infrared Survey Explorer* (*WISE*) images, although the nearby LkH*α* 316 and LkH*α* 316-neb become also quite strong by 25 µm.

Hillenbrand et al. (2012) saw a nebulosity closely associated with the *IRAS* source as well at the 2MASS *K* and *H* bands that they did not find at shorter wavelengths. We suggest that this gas feature can be seen at shorter than 2MASS wavelengths too (top right-hand panel of Fig. 8). At the wavelengths it is visible, it has a neat loop structure. The extent of this loop we measured from Pan-STARRS to *Herschel* images, and found to be 0.06–0.07 pc at the distance of 400 pc. This loop is rather thin and sharp, and the extent of it, from the compact source to the north-west corner, does not seem to vary with wavelength. These reflection nebulae around both hub centres indicate that there is interaction between the point sources and the cloud material.

4.5 CO outflow revisited

A large amorphous bipolar ^{12}CO outflow in NGC 2071-N was discovered by Fukui et al. (1986), and followed up by Iwata et al. (1988). They defined the outflow relatively old ($\tau \sim 1.7 \times 10^5$ yr) and suggested that its driving source is IRAS 05451+0037, although it is off-axis to the east from the outflow lobes. In this same study they also presented a higher resolution, though not fully calibrated CO map, where there is indication that the lobes are extended towards the *IRAS* source. They then suggested that the outflow has a U-shape with the *IRAS* source at the bottom of it. The redshifted CO lobe peaks nearly in between IRAS 05451+0037 and LkH*α* 316, which also complicates the interpretation with the *IRAS* source as the origin. Goldsmith et al. (1992) still found the origin of this outflow less clearly identifiable.

Then Aspin & Reipurth (2000) suggested their HH 472 jet and its unknown source to be the driving source of the outflow, as they are located between the blue and red lobes. This molecular outflow and the HH objects are also misaligned, perhaps indicating a stronger or differently directed flow in the past (Hillenbrand et al. 2012).

Interestingly, the complete loop-shaped nebulosity around IRAS 05451+0037 (Fig. 8) extends from the point source towards north-west, in which direction there is the apparent centre of the outflow, however from our fine-detailed ^{13}CO (1–0) molecular line data, plotting channel maps, we cannot confirm this outflow, and it is more probable that its south-east–north-west axis, interpreted at much lower resolution, corresponds to the dense features we can also see in column density along the south-east–north-west axis (e.g. Fig. 3, left).

5 CONCLUSIONS

We have presented *Herschel*, molecular line, and archival data sets, including 100 µm *Herschel* images, IRAM 30-m, and NRO 45-m observations over a newly resolved hub–filament structure in NGC 2071-North featuring a double centre. Our main results and conclusions are summarized as follows.

(i) We confirm that NGC 2071-North is part of the L1630-North complex at $d \sim 400$ pc, and is not affected by the Barnard's Loop (nearby in projection) that may be at a closer distance (∼180 pc).

(ii) The *Herschel* H_2 column density image reveals a $\sim 1.5 \times 1.5$ pc^2 size filamentary hub structure with curved arms, containing $\sim 500\,M_\odot$ above $A_V \sim 5$ mag. The 100 µm emission concentrates in the central part of the filament hub, at IRAS 05451+0037 and the emission star LkH*α* 316, and features diffuse lobes and loops around them.

(iii) We have estimated the energy balance by calculating gravitational and turbulent kinetic energy densities, as well as gravitational and internal pressures within 42 spots, with 25 arcsec radius, along the filaments. From these comparisons, together with finding several infall candidates in HCO^+ and $C^{18}O$, we conclude that gravity dominates on small scales, and NGC 2071-N is currently forming stars.

(iv) *Planck* POS magnetic field lines reveal a loop structure east of NGC 2071, extending up to NGC 2071-N. This results in east–west B-field lines in the east of the hub, and north–south running field lines in the west of the filament hub. This closely perpendicular B-field structure may be an efficient configuration for gathering material at this relatively isolated location.

(v) We suggest that a double centre could be formed in this hub, because the converging locations of two filament pairs are offset. This offset is 2.3 arcmin (0.27 pc) that also matches the diameter of a central hub ring that is seen in column density, traced by filaments, and in HCO^+ and HCN, which may indicate a transition and connection between the hub and the filaments.

(vi) We argue that not only two, but all of the three components of the LkHα 316 young star (along with 316-neb and 316/c) are in physical association due to the location of the latter at the junction of two filaments. We find that the clear gas loop feature around IRAS 05451+0037 can already be seen at shorter than 2MASS wavelengths. The extent of this loop we measured to be 0.06–0.07 pc that does not seem to vary with wavelength.

(vii) We have revisited the CO outflow, discovered by Fukui et al. (1986), and we do not seem to find its lobes in our high-resolution ^{13}CO data.

ACKNOWLEDGEMENTS

We thank the anonymous reviewer for their helpful and useful suggestions. VK thanks K. Pattle for useful discussions. VK and DW-T acknowledge Science and Technology Facilities Council (STFC) support under grant number ST/R000786/1.

This study has made use of data from the *Herschel* Gould Belt Survey (HGBS) project (http://gouldbeltherschel.cea.fr). The HGBS is a *Herschel* Key Programme jointly carried out by SPIRE Specialist Astronomy Group 3 (SAG 3), scientists of several institutes in the PACS Consortium (CEA Saclay, INAF-IFSI Rome and INAF-Arcetri, KU Leuven, and MPIA Heidelberg), and scientists of the *Herschel* Science Center (HSC).

This study is based on observations carried out with the IRAM 30-m Telescope under project number 030–13. IRAM is supported by INSU,CNRS (France), MPG (Germany), and IGN (Spain).

The 45-m radio telescope is operated by Nobeyama Radio Observatory, a branch of National Astronomical Observatory of Japan.

Funding for SDSS-III has been provided by the Alfred P. Sloan Foundation, the Participating Institutions, the National Science Foundation, and the U.S. Department of Energy Office of Science. The SDSS-III web site is http://www.sdss3.org/.

SDSS-III is managed by the Astrophysical Research Consortium for the Participating Institutions of the SDSS-III Collaboration including the University of Arizona, the Brazilian Participation Group, Brookhaven National Laboratory, Carnegie Mellon University, University of Florida, the French Participation Group, the German Participation Group, Harvard University, the Instituto de Astrofisica de Canarias, the Michigan State/Notre Dame/JINA Participation Group, Johns Hopkins University, Lawrence Berkeley National Laboratory, Max Planck Institute for Astrophysics, Max Planck Institute for Extraterrestrial Physics, New Mexico State University, New York University, Ohio State University, Pennsylvania State University, University of Portsmouth, Princeton University, the Spanish Participation Group, University of Tokyo, University of Utah, Vanderbilt University, University of Virginia, University of Washington, and Yale University.

The Pan-STARRS1 Surveys (PS1) and the PS1 public science archive have been made possible through contributions by the Institute for Astronomy, the University of Hawaii, the Pan-STARRS Project Office, the Max-Planck Society and its participating institutes, the Max Planck Institute for Astronomy, Heidelberg and the Max Planck Institute for Extraterrestrial Physics, Garching, The Johns Hopkins University, Durham University, the University of Edinburgh, the Queen's University Belfast, the Harvard-Smithsonian Center for Astrophysics, the Las Cumbres Observatory Global Telescope Network Incorporated, the National Central University of Taiwan, the Space Telescope Science Institute, the National Aeronautics and Space Administration under grant no. NNX08AR22G issued through the Planetary Science Division of the NASA Science Mission Directorate, the National Science Foundation grant no. AST-1238877, the University of Maryland, Eotvos Lorand University (ELTE), the Los Alamos National Laboratory, and the Gordon and Betty Moore Foundation.

This research has made use of "Aladin sky atlas" developed at CDS, Strasbourg Observatory, France.

SkyView has been developed with generous support from the NASA AISR and ADP programs (P.I. Thomas A. McGlynn) under the auspices of the High Energy Astrophysics Science Archive Research Center (HEASARC) at the NASA/GSFC Astrophysics Science Division.

DATA AVAILABILITY

The PACS and SPIRE maps, the *Herschel* column density and temperature maps, and the dense core lists extracted from them in the whole Orion B region are publicly available at the *Herschel* Gould Belt Survey Archive: http://gouldbelt-herschel.cea.fr/archives. Additional molecular line maps presented in this paper are available at https://doi.org/10.11570/23.0001.

REFERENCES

Alina D., Ristorcelli I., Montier L., Abdikamalov E., Juvela M., Ferrière K., Bernard J. P., Micelotta E. R., 2019, MNRAS, 485, 2825
André P. et al., 2010, A&A, 518, L102
André P., Di Francesco J., Ward-Thompson D., Inutsuka S.-I., Pudritz R. E., Pineda J. E., 2014, in Beuther H., Klessen R. S., Dullemond C. P., Henning T., eds, Protostars and Planets VI. Univ. Arizona Press, Tucson, AZ, p. 27
André P., Palmeirim P., Arzoumanian D., 2022, A&A, 667, L1
Anthony-Twarog B. J., 1982, AJ, 87, 1213
Arzoumanian D. et al., 2011, A&A, 529, L6
Arzoumanian D. et al., 2019, A&A, 621, A42
Aspin C., Reipurth B., 2000, MNRAS, 311, 522
Bally J., 2008, in Reipurth B., ed., Handbook of Star Forming Regions, Vol. I: The Northern Sky. Astron. Soc. Pac., San Francisco, p. 459
Benedettini M. et al., 2018, A&A, 619, A52
Bertoldi F., McKee C. F., 1992, ApJ, 395, 140
Bohlin R. C., Savage B. D., Drake J. F., 1978, ApJ, 224, 132
Bonnarel F. et al., 2000, A&AS, 143, 33
Bonnor W. B., 1956, MNRAS, 116, 351
Carter M. et al., 2012, A&A, 538, A89
Chambers K. C. et al., 2016, preprint (arXiv:1612.05560)
Chen C.-Y., King P. K., Li Z.-Y., 2016, ApJ, 829, 84

Claussen M. J., Wilking B. A., Benson P. J., Wootten A., Myers P. C., Terebey S., 1996, ApJS, 106, 111

Cutri R. M. et al., 2003, VizieR On-line Data Catalog: II/246

Dale J. E., Bonnell I., 2011, MNRAS, 414, 321

Dewangan L. K., Luna A., Ojha D. K., Anandarao B. G., Mallick K. K., Mayya Y. D., 2015, ApJ, 811, 79

Dhabal A., Mundy L. G., Rizzo M. J., Storm S., Teuben P., 2018, ApJ, 853, 169

Dunham M. K., Rosolowsky E., Evans, Neal J. I., Cyganowski C., Urquhart J. S., 2011, ApJ, 741, 110

Eisenstein D. J. et al., 2011, AJ, 142, 72

Evans, Neal J. I., 1999, ARA&A, 37, 311

Fiorellino E. et al., 2021, MNRAS, 500, 4257

Fukui Y., Sugitani K., Takaba H., Iwata T., Mizuno A., Ogawa H., Kawabata K., 1986, ApJ, 311, L85

Gaia Collaboration et al., 2018, A&A, 616, A1

Gibb A. G., 2008, in Reipurth B., ed., Handbook of Star Forming Regions, Vol. I: The Northern Sky. Astron. Soc. Pac., San Francisco, p. 693

Goldsmith P. F., Margulis M., Snell R. L., Fukui Y., 1992, ApJ, 385, 522

Greenfield P. et al., 2013, Astrophysics Source Code Library, record ascl:1304.002

Hacar A., Clark S., Heitsch F., Kainulainen J., Panopoulou G., Seifried D., Smith R., 2022, preprint (arXiv:2203.09562)

Hatchell J., Richer J. S., Fuller G. A., Qualtrough C. J., Ladd E. F., Chandler C. J., 2005, A&A, 440, 151

He Y.-X. et al., 2015, MNRAS, 450, 1926

Hillenbrand L. A., Knapp G. R., Padgett D. L., Rebull L. M., McGehee P. M., 2012, AJ, 143, 37

Iwata T., Fukui Y., Ogawa H., 1988, ApJ, 325, 372

Johnstone D., Di Francesco J., Kirk H., 2004, ApJ, 611, L45

Kirk H. et al., 2016, ApJ, 817, 167

Kirk H., Johnstone D., Di Francesco J., 2006, ApJ, 646, 1009

Koch E. W., Rosolowsky E. W., 2015, MNRAS, 452, 3435

Könyves V. et al., 2015, A&A, 584, A91

Könyves V. et al., 2020, A&A, 635, A34

Ladjelate B. et al., 2020, A&A, 638, A74

Lallement R., Vergely J.-L., Valette B., Puspitarini L., Eyer L., Casagrande L., 2014, A&A, 561, A91

Li H.-b., Fang M., Henning T., Kainulainen J., 2013, MNRAS, 436, 3707

Lyo A. R. et al., 2021, ApJ, 918, 85

Marsh K. A. et al., 2016, MNRAS, 459, 342

Megeath S. T. et al., 2012, AJ, 144, 192

Menten K. M., Reid M. J., Forbrich J., Brunthaler A., 2007, A&A, 474, 515

Miville-Deschênes M.-A., Murray N., Lee E. J., 2017, ApJ, 834, 57

Myers P. C., 2009, ApJ, 700, 1609

Myers P. C., Mardones D., Tafalla M., Williams J. P., Wilner D. J., 1996, ApJ, 465, L133

Nakamura F., Li Z.-Y., 2008, ApJ, 687, 354

Ochsendorf B. B., Brown A. G. A., Bally J., Tielens A. G. G. M., 2015, ApJ, 808, 111

Onishi T., Mizuno A., Kawamura A., Ogawa H., Fukui Y., 1998, ApJ, 502, 296

Palmeirim P. et al., 2013, A&A, 550, A38

Panopoulou G. V., Clark S. E., Hacar A., Heitsch F., Kainulainen J., Ntormousi E., Seifried D., Smith R. J., 2022, A&A, 657, L13

Pattle K. et al., 2015, MNRAS, 450, 1094

Peretto N. et al., 2012, A&A, 541, A63

Peretto N. et al., 2013, A&A, 555, A112

Peretto N., André P., Belloche A., 2006, A&A, 445, 979

Pilbratt G. L. et al., 2010, A&A, 518, L1

Pineda J. E. et al., 2022, preprint (arXiv:2205.03935)

Planck Collaboration XXXV, 2016, A&A, 586, A138

Rayner T. S. M. et al., 2017, A&A, 607, A22

Rygl K. L. J., Wyrowski F., Schuller F., Menten K. M., 2013, A&A, 549, A5

Sadavoy S. I., Shirley Y., Di Francesco J., Henning T., Currie M. J., André P., Pezzuto S., 2015, ApJ, 806, 38

Sault R. J., Teuben P. J., Wright M. C. H., 1995, in Shaw R. A., Payne H. E., Hayes J. J. E., eds, ASP Conf. Ser. Vol. 77, Astronomical Data Analysis Software and Systems IV. Astron. Soc. Pac., San Francisco, p. 433

Schlafly E. F. et al., 2014, ApJ, 786, 29

Schneider N. et al., 2010, A&A, 518, L83

Schneider N. et al., 2012, A&A, 540, L11

Shimajiri Y. et al., 2017, A&A, 604, A74

Skrutskie M. F. et al., 2006, AJ, 131, 1163

Snell R. L., 1989, in Tenorio-Tagle G., Moles M., Melnick J., eds, Proc. IAU Colloq. 120, Lecture Notes in Physics Vol. 350, Structure and Dynamics of the Interstellar Medium. Springer-Verlag, Berlin, p. 231

Soler J. D., 2019, A&A, 629, A96

Soler J. D., Hennebelle P., 2017, A&A, 607, A2

Soler J. D., Hennebelle P., Martin P. G., Miville-Deschênes M. A., Netterfield C. B., Fissel L. M., 2013, ApJ, 774, 128

Sousbie T., 2011, MNRAS, 414, 350

Tahani M., Plume R., Brown J. C., Kainulainen J., 2018, A&A, 614, A100

Tenorio-Tagle G., 1982, in Roger R. S., Dewdney P. E., eds, Astrophysics and Space Science Library Vol. 93, Regions of Recent Star Formation. Reidel, Dordrecht, p. 1

Traficante A., Fuller G. A., Billot N., Duarte-Cabral A., Merello M., Molinari S., Peretto N., Schisano E., 2017, MNRAS, 470, 3882

Treviño-Morales S. P. et al., 2019, A&A, 629, A81

Wouterloot J. G. A., Walmsley C. M., Henkel C., 1988, A&A, 203, 367

Zucker C., Speagle J. S., Schlafly E. F., Green G. M., Finkbeiner D. P., Goodman A. A., Alves J., 2019, ApJ, 879, 125

APPENDIX A: AVERAGED SPECTRA

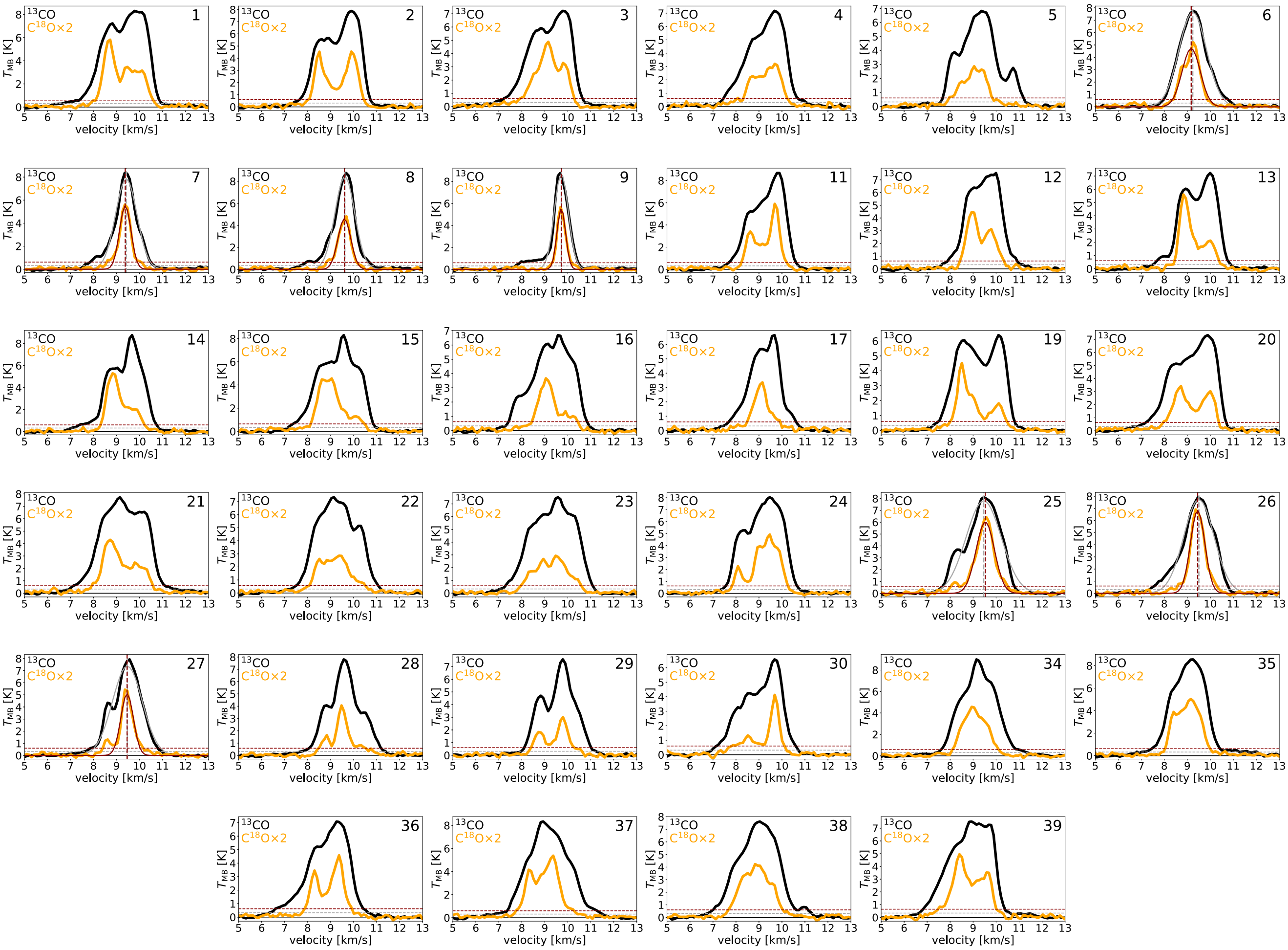

Figure A1. ^{13}CO (1–0) (black) and C^{18}O (1–0) (orange) spectra averaged over the analysis spots where observed (see Fig. 5). When it is reasonable, a Gaussian fit and its peak position are also included. Dashed horizontal lines mark 6σ rms thresholds; grey for the black spectra, and red for the overplotted profiles. For details, see Sections 3.3 and 3.4. Derived properties from these profiles are listed in Table 2.

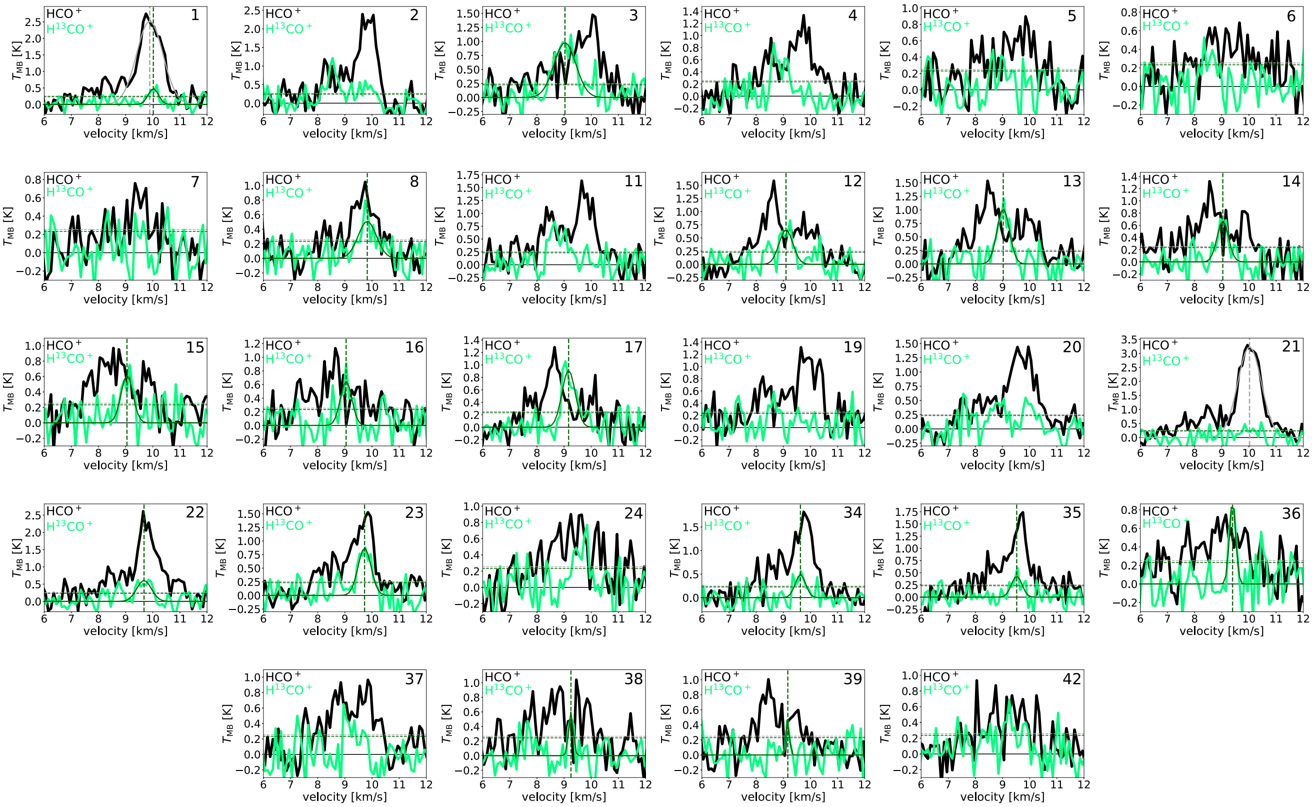

Figure A2. HCO$^+$ (1–0) (black) and H^{13}CO$^+$ (1–0) (light green) spectra averaged over the analysis spots where observed (see Fig. 5). When it is reasonable, a Gaussian fit and its peak position are also included. Dashed horizontal lines mark 3σ rms thresholds; grey for the black spectra, and green for the overplotted profiles. For details, see Sections 3.3 and 3.4. Derived properties from these profiles are listed in Table 2.

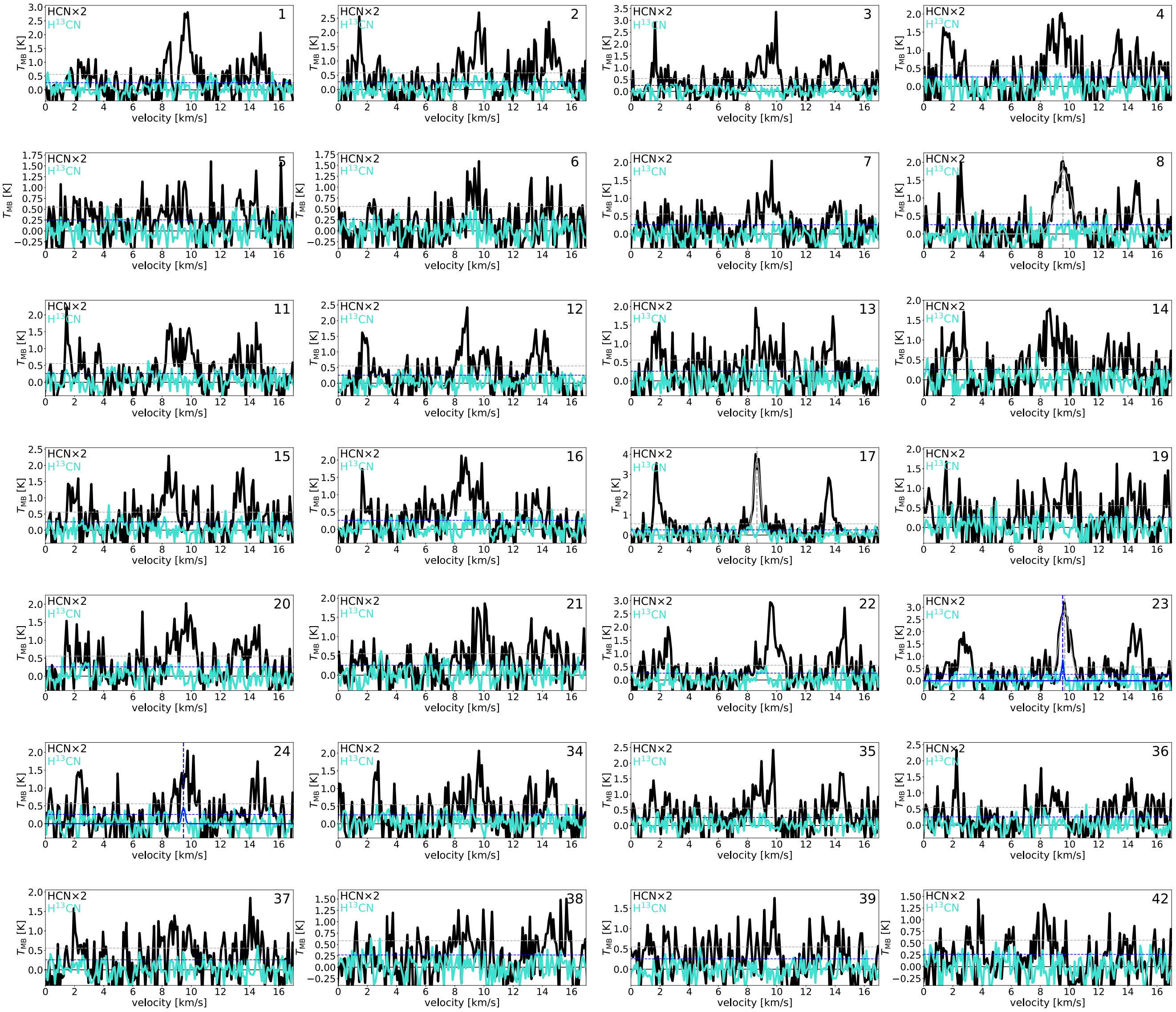

Figure A3. HCN (1–0) (black) and H^{13}CN (1–0) (cyan) spectra averaged over the analysis spots where observed (see Fig. 5). When it is reasonable, a Gaussian fit and its peak position are also included. Dashed horizontal lines mark 3σ rms thresholds; grey for the black spectra, and blue for the overplotted profiles. For details, see Sections 3.3 and 3.4. Derived properties from these profiles are listed in Table 2.

APPENDIX B: INTEGRATED INTENSITY MAPS

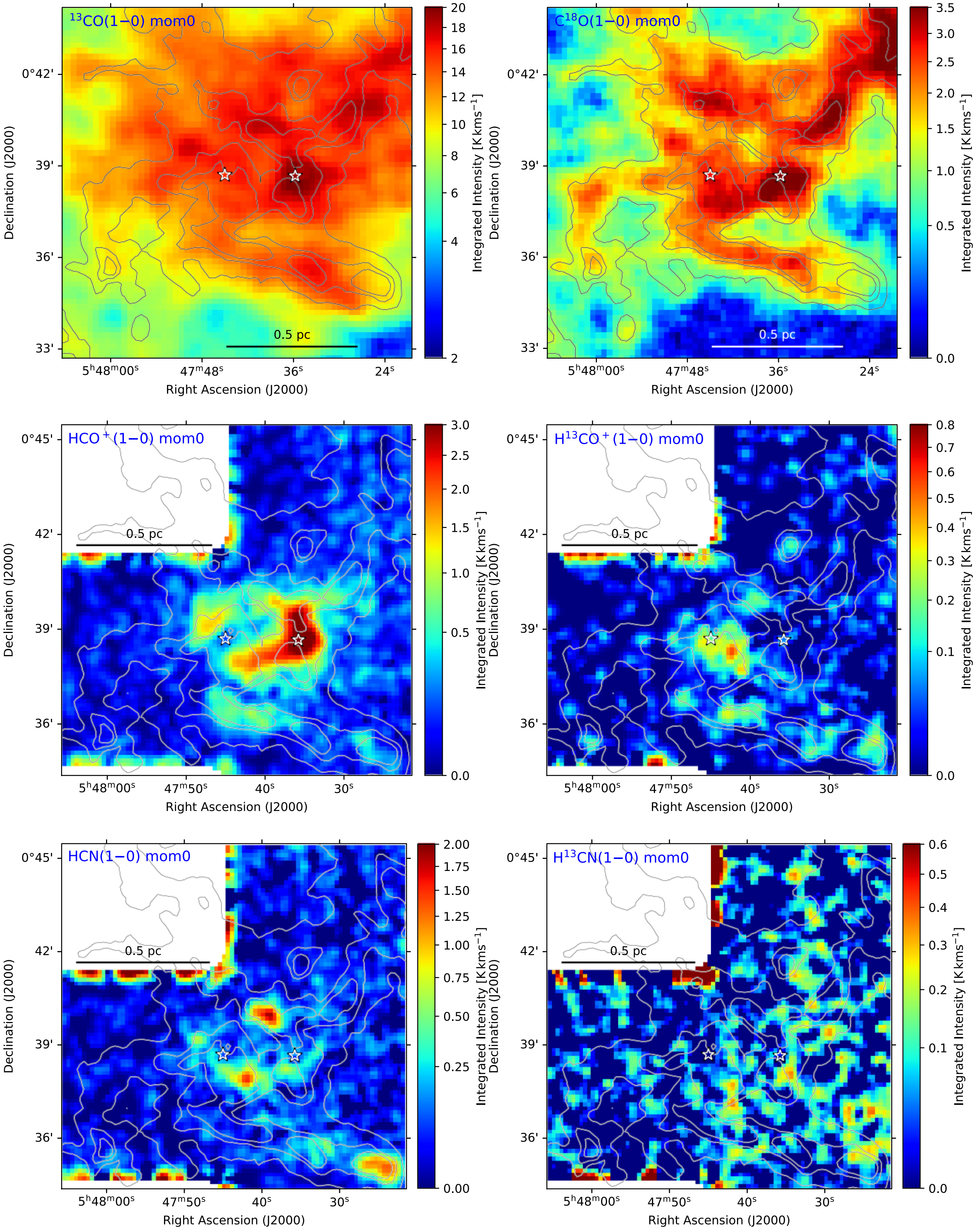

Figure B1. Integrated intensity (moment 0) maps of the hub centre (in main beam temperature) in the molecular lines indicated in the upper left-hand corner. Higher intensity ‘strings of beads’ at the map edges are artefacts. In all panels smoothed column density contours are overplotted, and the left- and right-hand white stars mark the locations of IRAS 05451+0037 and LkHα 316, respectively.

This paper has been typeset from a TEX/LATEX file prepared by the author.